



LAWRENCE
LIVERMORE
NATIONAL
LABORATORY

UCRL-TR-215943

The Feasibility of Cask "Fingerprinting" as a Spent-Fuel, Dry-Storage Cask Safeguards Technique

K. P. Ziock, P. Vanier, L. Forman, G. Caffrey, J. Wharton, A. Lebrun

October 5, 2005

Disclaimer

This document was prepared as an account of work sponsored by an agency of the United States Government. Neither the United States Government nor the University of California nor any of their employees, makes any warranty, express or implied, or assumes any legal liability or responsibility for the accuracy, completeness, or usefulness of any information, apparatus, product, or process disclosed, or represents that its use would not infringe privately owned rights. Reference herein to any specific commercial product, process, or service by trade name, trademark, manufacturer, or otherwise, does not necessarily constitute or imply its endorsement, recommendation, or favoring by the United States Government or the University of California. The views and opinions of authors expressed herein do not necessarily state or reflect those of the United States Government or the University of California, and shall not be used for advertising or product endorsement purposes.

This work was performed under the auspices of the U.S. Department of Energy by University of California, Lawrence Livermore National Laboratory under Contract W-7405-Eng-48.

The Feasibility of Cask “Fingerprinting” as a Spent-Fuel, Dry-Storage Cask Safeguards Technique

Klaus Ziock

Lawrence Livermore National Laboratory

Peter Vanier and Leon Forman

Brookhaven National Laboratory

Gus Caffrey, Jason Wharton

Idaho National Laboratory

Alain Lebrun

International Atomic Energy Agency

Abstract

This report documents a week-long measurement campaign conducted on six, dry-storage, spent-nuclear-fuel storage casks at the Idaho National Laboratory. A gamma-ray imager, a thermal-neutron imager and a germanium spectrometer were used to collect data on the casks. The campaign was conducted to examine the feasibility of using the cask radiation signatures as unique identifiers for individual casks as part of a safeguards regime. The results clearly show different morphologies for the various cask types although the signatures are deemed insufficient to uniquely identify individual casks of the same type. Based on results with the germanium spectrometer and differences between thermal neutron images and neutron-dose meters, this result is thought to be due to the limitations of the extant imagers used, rather than of the basic concept. Results indicate that measurements with improved imagers could contain significantly more information. Follow-on measurements with new imagers either currently available as laboratory prototypes or under development are recommended.

Table of Contents

1.	Introduction	1
2.	Introduction to coded aperture imaging	2
3.	Instrumentation	4
	a. Gamma-ray imager	4
	b. Thermal-neutron imager	5
	c. Gamma Spectrometer	6
4.	Tan Facility	7
5.	Measurements	8
	a. Cask 1: Westinghouse MC-10	8
	i. Gamma-Ray Images	8
	ii. Germanium Spectrometer Data	10
	iii. Neutron Images	10
	b. Cask 2: NuPac 125B	11
	i. Gamma-Ray Images	11
	ii. Germanium Spectrometer Data	11
	iii. Neutron Image	11
	c. Cask 3: GNS V/21	11
	i. Gamma-Ray Images	11
	ii. Germanium Spectrometer Data	13
	iii. Neutron Image	13
	d. Cask 4: REA-2023	13
	i. Gamma-Ray Images	13
	ii. Germanium Spectrometer Data	14
	iii. Neutron Image	14
	e. Cask 5: VSC-17	15
	i. Gamma-Ray Images	15
	ii. Germanium Spectrometer Data	16
	iii. Neutron Image	17
	f. Cask 6: TN-24P	17
	i. Gamma-Ray Images	17
	ii. Germanium Spectrometer Data	17
	iii. Neutron Image	17
6.	Discussion	17
	a. Gamma-Ray Results	18
	b. Ideal Gamma-Ray Imager	23
	c. Neutron Results	23
7.	Conclusions	24
8.	Recommendations	24
9.	Acknowledgements	24
10.	References	24

Table of Figures

Figure 1:	Six casks	1
Figure 2:	Schematic coded-aperture imager	2
Figure 3:	Gamma-ray imager	3
Figure 4:	Sample gamma-ray image	3
Figure 5:	Zero-threshold gamma-ray image	4
Figure 6:	Thermal-neutron imager	5
Figure 7:	Polyethylene block neutron source photograph	6
Figure 8:	Polyethylene block neutron source neutron image	6
Figure 9:	Polyethylene block neutron source simulation	6
Figure 10:	Germanium spectrometer	7
Figure 11:	TAN cask layout	7
Figure 12:	Cask 1 wide-angle gamma-ray image	10
Figure 13:	Cask 1 zoomed gamma-ray image	10
Figure 14:	Cask 1 second wide-angle gamma-ray image	11
Figure 15:	Cask 1 overhead gamma-ray image	11
Figure 16:	Gamma-ray imager on lift	11
Figure 17:	Cask 1 spectrum	12
Figure 18:	Cask 1 neutron image	12
Figure 19:	Cask 1 histogram of neutron image	12
Figure 20:	Cask 1 smoothed neutron image	12
Figure 21:	Cask 2 spectrum	13
Figure 22:	Cask 3 gamma-ray image	13
Figure 23:	Cask 3 spectrum	14
Figure 24:	Cask 3 15-hour neutron image	14
Figure 25:	Cask 3 neutron image with 1 hour of anti-mask data	14
Figure 26:	Cask 4 gamma-ray image	15
Figure 27:	Cask 4 spectrum	15
Figure 28:	Cask 4 neutron image	15
Figure 29:	Cask 4 histogram across neutron image	15
Figure 30:	Cask 5 wide-angle gamma-ray image	16
Figure 31:	Cask 5 zoomed gamma-ray image	16
Figure 32:	Cask 5 spectrum	16
Figure 33:	Cask 5 high-resolution neutron image	17
Figure 34:	Cask 5 smoothed high-resolution neutron image	17
Figure 35:	Cask 5 low-resolution neutron image	17
Figure 36:	Cask 6 spectrum	18
Figure 37:	Cask 6 neutron image	18
Figure 37:	Wide angle gamma-images with histograms	19

Table of Tables

Table 1:	Cask load summaries	8
Table 2:	Cask image cross-reference	9
Table 3:	Cask spectral results	20

Introduction

Accounting for spent nuclear fuel is one of the important safeguarding tasks performed by the IAEA. The material is both highly radioactive and can contain significant quantities of fissile material. For the ten years following the last burn cycle, the material is generally stored in wet-storage facilities or “ponds” at the reactor site. After this time, it can be transferred to dry storage casks and moved to pads awaiting final disposal. Despite the fact that we are over five decades into the nuclear era, no long-term disposal sites exist. This means that more and more material is accumulating at “temporary” storage facilities in dry storage casks.

Although there are many types of dry storage casks, they all share the basic design goal to limit radiation exposure outside the cask. This means that cask walls include significant shielding for both neutron and gamma-radiation. Hence, traditional non-destructive analysis (NDA) and assay techniques to verify cask contents are ineffective after a cask is sealed. The safeguard regime therefore relies on the use of tags and seals (C/S) with regular inspections to maintain continuity of knowledge that cask contents remain as loaded.

The casks are loaded in the presence of IAEA inspectors by the reactor operators and “irreversibly” sealed. Tamperproof tags and seals (C/S) are added by the inspectors. The casks are then moved to a storage “farm” where many casks are stored. Periodic inspection of the tags and seals is currently the only technique that exists to certify that the cask contents have not been altered. As the inventory of spent fuel increases around the world, monitoring of cask loading operations and subsequent tags and seals inspections are creating a greater burden on IAEA resources.

The ever-increasing quantity of casks requiring regular inspection increases the likelihood that tags and seals will fail. This is particularly problematic since the casks are generally stored out of doors, exposed to the weather. In the event of C/S failure, there is currently

no means of reestablishing a cask’s contents without reopening it. This technique is not considered realistic in light of the costs associated with such an undertaking.

In the late winter of 2003, the IAEA held a working-group meeting of experts to examine the means of safeguarding spent nuclear fuel. The panel focused on both wet and dry storage facilities. One of the suggestions made in the subsequent report [1] was to examine the idea of “fingerprinting” as a means to re-certify the contents of a cask in the event of C/S failure and also as a means of strengthening the C/S regime itself. The general concept relies on identifying cask properties that can be used to uniquely establish a cask ID and that the contents of that cask have not been significantly altered.

At the heart of the technique are the facts that the casks are loaded with fuel assemblies of varying burn-up and that radiation from the fuel reaches the cask surface despite the heavy shielding used in cask construction. The amount and type of radiation emitted by the fuel assemblies is known to be a function of their burn-up. In the loading process, the more heavily-used fuel elements are distributed throughout the cask to distribute the heat load within the cask. In principle, this should result in a multi-lobe signature of the radiation field.

It is expected that some vestige of the radiation pattern will survive to the cask surface. The pattern will have two components. The first and major constituent will be due to radiation that interacts in the cask walls on the way to the surface. This radiation will generate a diffuse image, such as that obtained from a light bulb behind a glass diffuser. The second, smaller, component of the radiation field will exit the cask without interacting with the cask at all. This radiation will provide a faithful rendition of the geometry of the outer nuclear materials. (The inner fuel elements will be shielded by the outer layers and will be difficult to image directly.)



Fig. 1 Six casks at TAN facility INL.

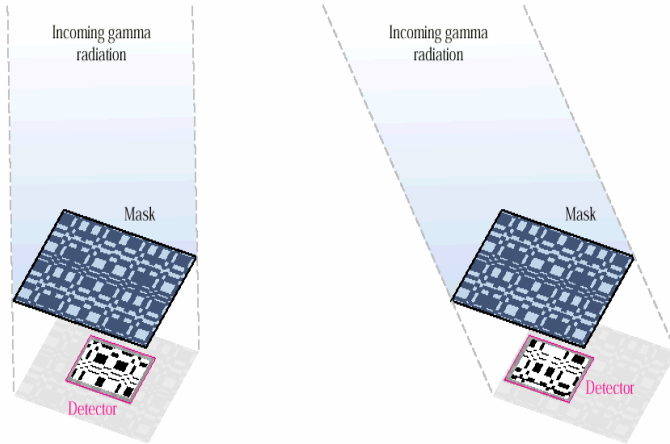


Fig. 2. Schematic representation of a coded aperture imager. Plane-parallel radiation coming from different directions, projects different parts of the mask pattern onto the detector. The detector sized portions of the mask are unique and do not interfere with each other.

It is thought that the overall radiation pattern can be used as an important constituent of the cask “fingerprint.” Further it was suggested that this radiation field could be measured with the use of radiation imaging instruments.

Based on these recommendations, a measurement campaign including both a thermal neutron[1] and gamma-ray imager[2] was undertaken at Idaho National Laboratory (INL.) At the Test Area North (TAN) site of INL, there are six different spent fuel casks (see Fig. 1.) This report documents the results obtained during this campaign and makes recommendations for future work on this concept.

Introduction to coded aperture imaging

The penetrating nature of the gamma-rays and neutrons that allows them to be detected outside of a cask also makes constructing an imager for these types of radiation difficult. In addition to a source of radiation, to generate an image generally requires a position-sensitive detector and a focusing optic. The former can be difficult to fabricate, the latter, save for a pin-hole camera, is impossible with current technologies.

The problem with a pin-hole camera is that it makes an image by rejecting all but a small fraction of the radiation incident on an instrument. Fortunately, the efficiency of the pin-hole camera can be increased by piercing the blocking surface with more than one hole. This has the advantage that more radiation reaches the detector, decreasing the imaging time. It has the disadvantage that each hole generates its own image and these images will overlap for all but the simplest

scenes. In the limit, where a large fraction of the blocking sheet is pierced ($\sim 50\%$) it is best to think in terms of the shadow pattern that is created. Then, an ideal multiple pin-hole camera must have two attributes: 1) a unique shadow pattern must be cast onto the detector by a point source in each pixel of the field-of-view and 2) the shadow patterns for different pixels in the field of view must not interfere with each other, i.e. they must be “orthogonal.” Such patterns were perfected in the 1970’s by the high energy astrophysical community and are called coded apertures. They are described in more detail in [3-5].

A schematic representation of a coded aperture imager is given in Fig. 2. The shadow mask is placed a focal length (f) in front of a position-sensitive detector. The mask must be largely opaque to the radiation to be imaged and has four times the area of the detector. It is made of a four-fold replication of a base pattern called a uniformly redundant array (URA). A source in a given pixel of the field of view will project one of the detector-sized patterns on to the detector. Each such pattern is unique, allowing one to determine where a source is located. The patterns are also orthogonal in the sense that the URA pattern auto-correlates to a delta function. Hence a faithful image can be generated mathematically from the pattern encoded at the detector.

For a base pattern $r \times s$ in size, (mask $2r \times 2s$) there will be $r \times s$ unique detector-sized patterns giving a field of view of $r \times s$ pixels. Generally, it is desirable to over sample the mask pattern by at least a factor of 2 (i.e. the detector pixels are one quarter the area of a mask pixel.)[5] The angular resolution of the imager is the size of the base mask element, a , divided by the focal length, f . To obtain a position resolution at the source one multiplies the angular resolution by the distance to the source, d , hence:

$$\Delta X = \frac{a}{f} d .$$

Of concern in coded aperture imaging is that the image is encoded as a variation in counts as a function of position across the detector face. Anything that produces such a variation leads to structures in the image. If the variations are not from the shadow of the mask pattern, the structures in the image will be artifacts and not representative of the radiation field in the field of view. Fortunately, a simple technique exists to measure such modulations without compromising accumulation time.[5, 6]

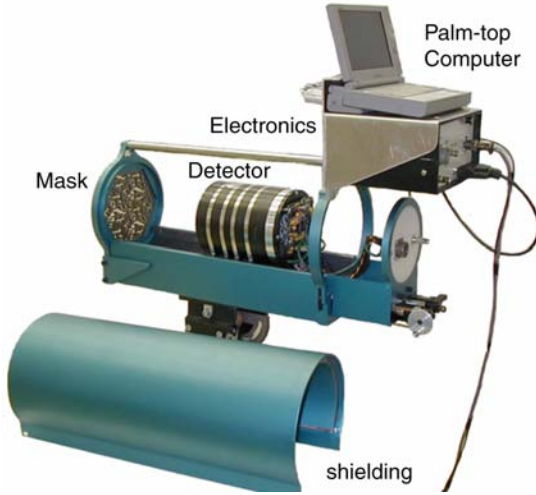


Fig. 3. Current-generation imager. The unit is battery powered and provides variable zoom images.

Some families of the coded apertures (hexagonally uniformly redundant arrays, HURA [7] and modified uniformly redundant arrays, MURA [8]) are anti-

symmetric when rotated about their central pixels by a fixed amount (60 and 90 degrees for the HURA and MURA, respectively). With knowledge of this property, the image can be taken in two sessions, one with the “mask” orientation of the shadow mask and one with its inverse or “anti-mask” orientation. When added together, the resulting data set has no modulation from the mask pattern. Therefore, any modulation must be spurious and can be removed before the mask and anti-mask data are deconvolved separately and added together to form the final image. This procedure makes the coded-aperture technique very robust, providing faithful images in high background environments.

There is a penalty inherent to coded aperture imaging when compared to direct imaging techniques. To unfold the image requires using all of the data in the detector to generate each pixel of the image. This means that the standard deviation of the statistical noise in each pixel is the square-root of the total number of counts in the detector as a whole. This is higher than in a “true-imager” where the radiation from one direction over the entire instrument aperture is concentrated onto the detector with the use of a lens or other imaging optic. In

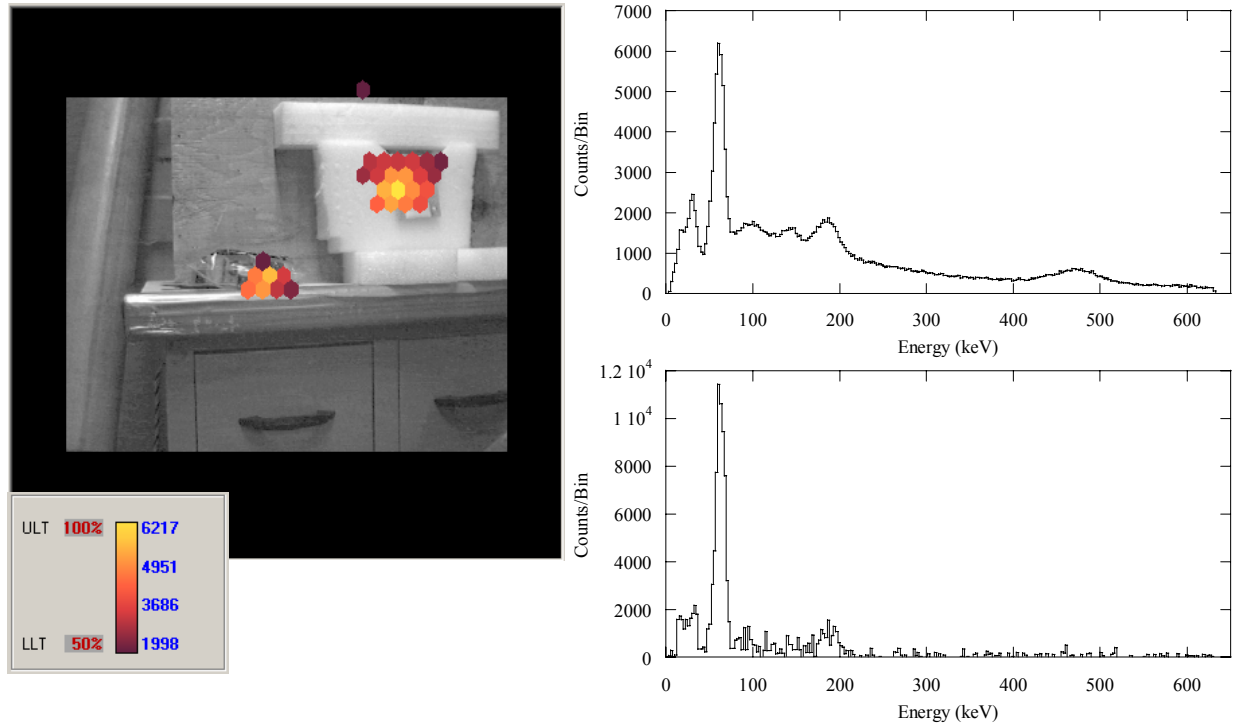


Fig. 4. The standard gamma-ray imager data as it is presented in the report. The image is of two point sources taken with the gamma-ray imager after it was unpacked at INL. The two sources are HEU (left) and ^{241}Am (right.) The gamma-ray image is scaled to the video image and pixels below 50% peak intensity are turned clear so that the visible-light image can be seen for reference. This data was taken with the widest gamma-ray field of view. In such data, the field of view of the visible light image is less than that of the gamma-ray image; hence the black border about the visible light image. The top spectrum is from all of the events collected by the imager. The lower spectrum is just for the gamma-ray pixels that are colored (above the 50% threshold.) As seen, the latter spectrum can differ significantly from the total spectrum. This is further exemplified in Fig. 5.

that case the standard deviation in each pixel of the image is the square-root of the counts in just that pixel of the detector. As a consequence, the advantage of a coded-aperture imager over a pin-hole camera is best for a point source, when only a single pixel in the field of view is bright. In this situation, the advantage in signal-to-noise ratio over the pin-hole is given by the square root of the number of open pixels in the base pattern. As more of the field of view glows from extended sources, the advantage decreases until, in the limit where the whole field of view glows, the sensitivity reverts to approximately that of the pin-hole camera.[4]

An additional property of coded aperture imagers that one must consider in this application is the confusing effect of partially encoded sources. Because the mask pattern is a replication of the base pattern, a source that falls outside the primary field of view will be imaged at the wrong location. Specifically, it will appear on the opposite side with some additional noise spread throughout the image. Although this problem can be successfully removed through the inclusion of suitable detector collimation, neither of the imagers described below makes use of this technique.

Instrumentation

The cask measurements reported below were conducted using a thermal neutron and a gamma-ray imager. Both

of these instruments form images using the coded-aperture technique described above. However, they differ significantly in the position-sensitive detectors, mask and shielding materials required by their respective radiation types. The specifics of each instrument are described in more detail below. In addition to the imagers, a collimated coaxial germanium detector was used to determine the gamma-ray spectrum from each of the casks. The details of this system are also provided below.

Gamma-Ray Imager

The gamma-ray imager used in these measurements is shown in Fig. 3 and is described in detail in Zioc and Nakae.[2] It comprises a base-19, HURA, coded-aperture mask used to project a shadow pattern onto a CsI(Na)-based, position-sensitive, gamma-ray detector. The mask is 5 mm thick Ta with a hexagonal hole size of 2.14 mm per flat face. The detector uses a 12-cm diameter, one-centimeter thick CsI(Na) disk to convert incident gamma-rays to a flash of scintillation light. The CsI is mounted on a Hamamatsu R3292 [9] position-sensitive-photomultiplier tube (PSPMT). The location and energy of each gamma-ray event is determined by measuring and centroiding the scintillation light flash as described in [2]. The position resolution of the detector is ~ 3 mm and the energy resolution is $\sim 11\%$ at 356 keV. The detector is mounted on linear bearings that allow it to be moved and set in one of five different

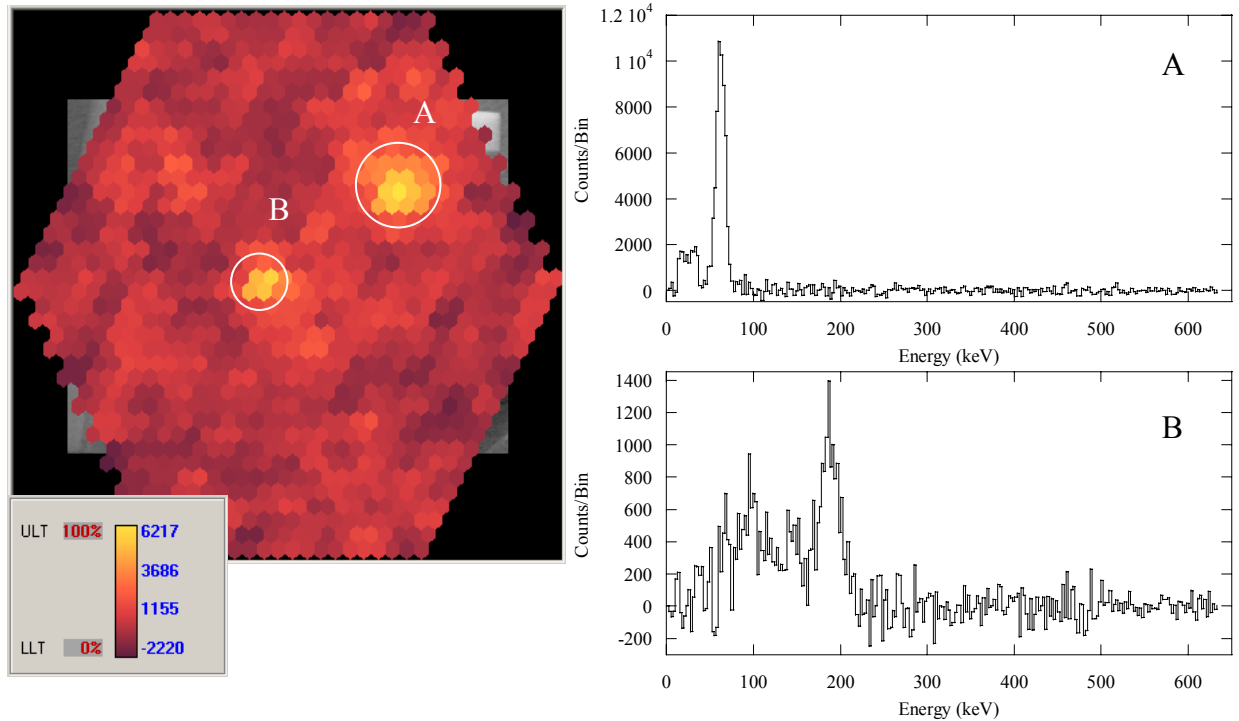


Fig. 5. Same data as Fig. 4, but with the gamma-ray image threshold set to zero. The hexagonal field of view of the imager is readily apparent. The spectra on the right are from the yellow pixels within each of the circles. This clearly identifies the Am source as source A and source B as the HEU.

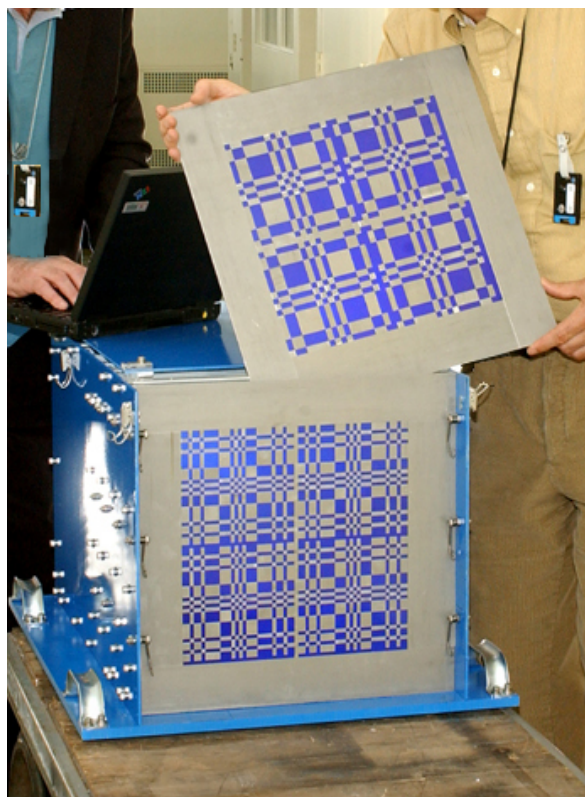


Fig. 6. Code-aperture, thermal-neutron imager.

focal lengths from the mask, providing a zoom capability. Data from the PSPMT is collected by a gated-integrator-based data acquisition system that uses a commercial, 16-bit digitizer mounted in a palm-top computer. The computer records the data in list-mode and also generates an online image that is periodically updated.

As discussed above, the data is collected in two, equal-time integrations, one in the “mask” and one in the “anti-mask” orientation. A 60-degree rotation of the mask must be performed between the two integrations.

In addition to the gamma-ray data, a visible-light video camera, coaligned with the imaging axis of the instrument, is used to record a visible-light image before each run. Based on the measured distance to the source, the visible-light image is scaled to the gamma-ray image and the two are simultaneously displayed in an overlay mode on the computer screen. The gamma-ray image is shown in false-color “in front” of the visible-light image. Those gamma-ray pixels a selectable-value below the maximum are turned clear so that portions of the visible-light image can be seen (Fig. 4). Up to four energy regions-of-interest may be set before a run. Separate images are made in each of these energy bands and in the overall spectrum during the run.

The list-mode data file recorded during an acquisition includes all of the information available about each gamma-ray event. Hence, a complete post-acquisition analysis can be performed with these data files allowing the user to vary software settings (such as source distance and energy cuts) as if these changes were made during the actual acquisition. In addition to the on-line displays that are generated as data is accumulated (or replayed,) a separate detector record is maintained for each energy bin of the imager. Upon completion of an acquisition, these can be individually deconvolved to create a separate image for each energy bin. The resulting data-cube is used to interactively determine both the images obtained with different energy cuts on the data, and the spectrum from different pixels or regions of the image (Fig. 5.) [10]

Finally, it should be noted that the gamma-ray imager used in these measurements is a prototype instrument developed for use in arms-control applications. As such, it is optimized to respond to gamma-radiation from highly-enriched uranium (HEU) at 186 keV and the 374 and 414 keV lines from plutonium. In addition, it provides excellent response at the ~ 100 keV K-shell fluorescence radiation from these elements. Unfortunately, the upper limit of the electronics is set to 630 keV, a value that is too low to image any of the line radiation that was measured to leak from the casks with the Ge spectrometer.

Thermal-Neutron Imager

The thermal neutron imager is based on a crossed-wire chamber with a 20-cm x 17-cm sensitive area operated in the proportional mode with a gas mixture of 6 bar of ^3He and 2.5 bar of propane. Details of the construction and the readout electronics can be found elsewhere [11]. The detector chamber is enclosed in a cadmium-lined box equipped with one of three choices of coded-aperture, MURA masks fabricated from 0.4-mm thick cadmium pixels mounted on an unperforated aluminum backing sheet. A mask can be inserted in one of four different tracks at different focal lengths, and can be used as its own anti-mask by rotating through a right angle about the optic axis before insertion into the track. The base pattern of each mask is a square of 15 cm x 15 cm, and the three masks available consist of (A) 19 x 19 (B) 31 x 31 and (C) 47 x 47 pixels in the base pattern, with four copies tiled to make each a complete mask. For most of the data in this report, the focal length is 10 cm, and the width of the field of view at the source is therefore 1.5 times the distance to the cask. The imager is shown in Fig. 6.

A custom-built, data-acquisition board is used to accumulate a 2-dimensional spatial histogram of neutron absorption events. The histogram consists of a 608 x



Fig. 7. Test of neutron imager in the laboratory using three PE cubes with ^{252}Cf sources embedded in the top and bottom cubes

512 array of 32-bit integers that can be zeroed or read out at any time by the controlling laptop computer through a 32-channel, digital, PCMCIA interface.

The spatial resolution of the chamber is limited to about 1 mm by the difference in ranges of the proton and triton produced by the reaction of a neutron with ^3He , because the recoil direction is not determined. Nevertheless, the readout electronics oversamples the resolution elements by about a factor of 3 in both x and y. The smallest mask pixel (3 mm x 3 mm) is consequently oversampled by about a factor of 9 in each direction. (The detector has far better resolution than is needed for this application because it was originally designed for a different purpose – protein crystallography with cold neutron beams.) This oversampling provides a high

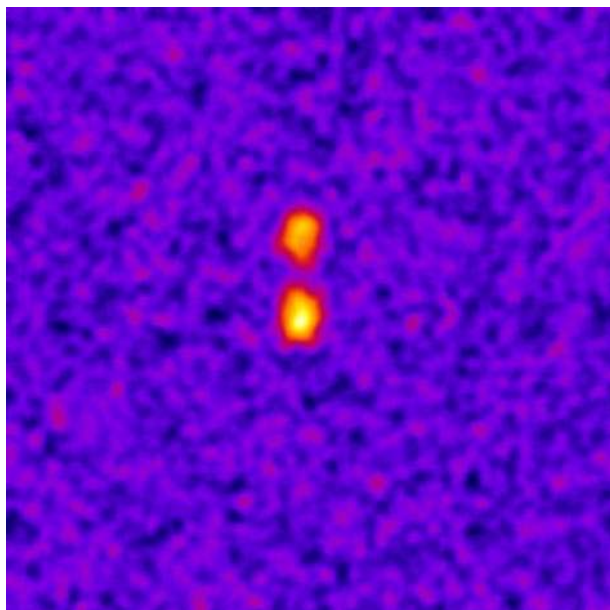


Fig. 8. Thermal neutron image of configuration in Fig 7, acquired in 10 minutes using the 47 x 47 MURA mask

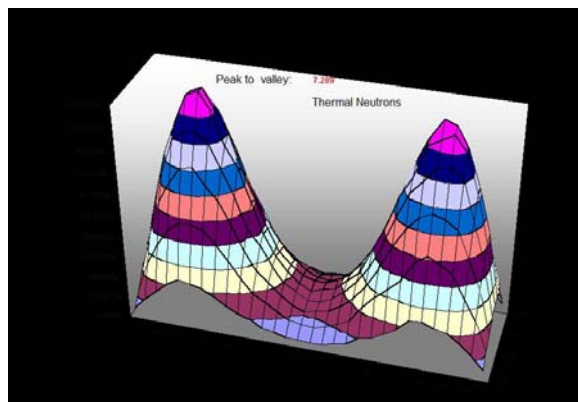


Fig. 9. Monte Carlo simulation of thermal neutron leakage from three cubes containing two sources

degree of adjustability in the image-processing software, which allocates regions of the detector to pixels of the mask shadow while taking account of the magnification of the shadow at short ranges. Optimizing the focus for objects in the scene at different ranges can therefore be performed by software after the data are recorded. Also, physical registration of detector elements with mask pixels is not required.

Laboratory tests of the imager at INL before deployment at the TAN facility demonstrated the resolution and contrast that can be achieved with ideal thermal neutron sources. Two ^{252}Cf spontaneous fission sources were embedded at the centers of cubes of high density polyethylene (PE) of dimensions 10 cm on the side. These moderating cubes were stacked with another cube between them, as shown in Fig. 7.

The resulting neutron image, shown in Fig. 8, was obtained using the C-mask at a range of 3 m with a focal length of 30 cm. The image is consistent with a range of ~ 5 cm for 2 MeV neutrons in PE. Thermal neutrons leak preferentially from the centers of the faces of the cubes holding the sources, and do not fill the three cubes uniformly.

The configuration was modeled by Alain Lebrun using a Monte Carlo code (see Fig. 9.) The lack of thermal neutrons emitted from the face of the center cube is a consequence of the fact that the thermalization distance of the fission neutrons is somewhat less than 5 cm in PE, and the diffusion length for thermal neutrons is considerably less than 5 cm. Therefore, the maximum intensity is seen at the center of the face of each cube that contains a source.

Gamma spectrometer

The high-resolution gamma-ray spectra recorded for the casks were taken using a 39% relative-efficiency, N-

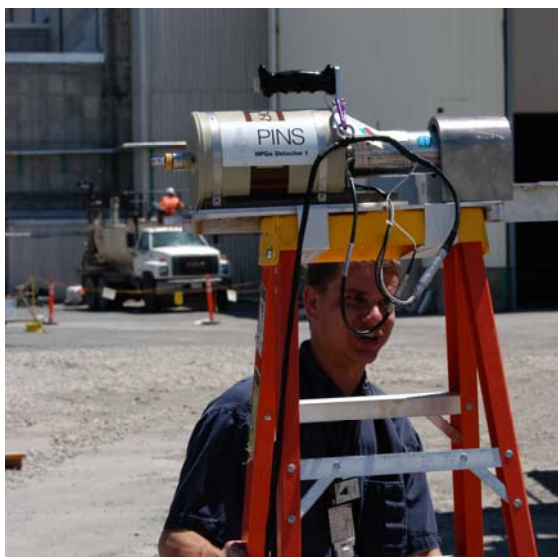


Fig. 10. The Ge spectrometer and collimator.

type, coaxial, high-purity, germanium detector. It is collimated with a bismuth annulus restricting its field of view to 10 degrees. The system is the same as used for PINS work and has been described in detail elsewhere [12]. The data were collected using an ORTEC Nomad-Plus, portable, multi-channel analyzer. The deadtime of the measurements was kept below 26%. Data were collected from a distance of 3 m and the detector was elevated 1.8 m above the ground, at approximately cask mid-height. The system is shown *in situ* in Fig. 10.

TAN facility

The “Test Area North” at Idaho National Laboratory (INL) has a facility to perform experimental measurements on six different, spent-nuclear-fuel, dry-storage casks. These are set out doors on a concrete pad meas-

uring 28.6 x 12.9 m (Fig. 1 and 11). A fence surrounding the edge of the pad provides a personnel boundary between the general and a radiation zone. Flux at the boundary can be as high as 5 mR/hr. At a neighboring location, fuel and components from the Three Mile Island reactor are stored.

The following casks are located on the concrete pad. Details of loading are obtained from [13]:

- 1) Westinghouse MC-10. This cask contains 5 intact Turkey Point PWR assemblies, 12 VEPCO PWR assemblies and one BCD B-17 PWR assembly. The latter has 21 fuel rods replaced by stainless steel rods for a total of 183 fuel rods. Thus 18 of 24 possible locations are used for a total of 14.99 Metric Tons of Heavy Metal (MTHM).
- 2) NuPac 2125-B Cask. This cask contains Three Mile Island Reactor 2 debris canisters in two of 7 locations. The cask contains a total of 0.02 MTHM.
- 3) GNS Castor V/21 Cask. This Cask contains 21 VEPCO PWR assemblies. Twenty of the assemblies are intact while one has 12 rods removed for a total of 9.27 MTHM. The fuel was discharged from the Surry reactor in November 1981 and was in water storage until 7/85 when it was loaded into the cask.[14] On average it has a burn-up of 30-35 GWd/MTU.[15]
- 4) REA-2023. This cask is loaded with commercial spent nuclear fuel comprising intact assemblies from Connecticut Yankee (PWR,) H. B. Robinson (PWR,) Beach Bottom (BWR) and Dresden I (BWR) reactors. Five positions in the cask are occupied by “loose” fuel rods.

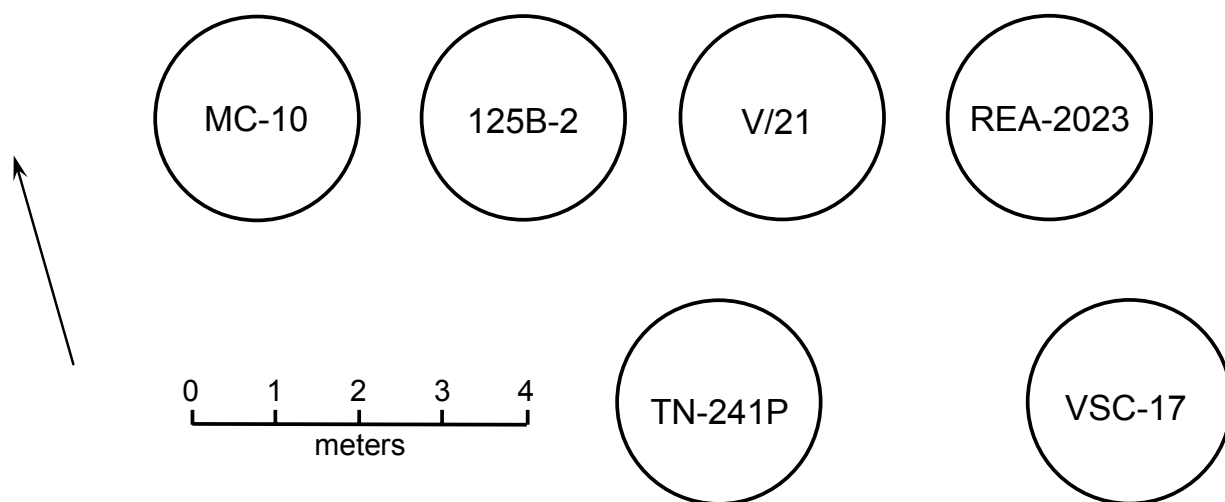


Fig. 11. Layout of the casks at the TAN facility.

The cask also contains fuel from the Loss of Fluid Test (LOFT) reactor including the center module FP-1 with two rods removed and the remains of the FP-2 center module housed in ten storage cans that also contain two loose FP-rods and epoxy. The total Cask contents is 1.79 MTHW

- 5) Pacific Sierra Nuclear VSC-17 Cask. This cask contains fuel from the Dry Rod Consolidation Technology project (DRCT.) The canisters are each loaded with the fuel from two fuel assemblies. These were extracted from standard Westinghouse 15 x 15 zircalloy clad fuel assemblies from VEPCO and Turkey Point reactors. The cask contains a total of 5.31 MTHM.
- 6) Transnuclear TN-24P Cask. This cask contains seven DRCT canisters each with the fuel of two normal assemblies (see cask 5 above.) It also contains 12 LOFT assemblies for a total of 8.04 MTHM.

The contents of the various casks is summarized in Table 1.

Measurements

The details of measurements and results for each cask are presented below. The gamma-ray image for each viewing angle and zoom is presented together with the associated energy spectrum. The threshold on the gamma-ray image is set at 50% for all but cask 3 where 60% was used due to the high noise level of the image. A summary of the images is given in Table 2.

Cask 1: Westinghouse MC-10

Gamma-ray images

This cask is the first one measured with the gamma-ray imager because the instrument could be positioned so that no other cask was in the imager's immediate field of view. To achieve this, the instrument was placed on the east side of the pad, close enough to the cask so that it hid the other casks. The cask's location did mean that radiation from the neighboring pad containing waste from the Three Mile Island reactors entered the back of the imager. This was noted as a reduction in the instantaneous count rate from ~ 3100 c/s to ~ 2600 c/s when the operator stood behind the instrument. To reduce this rate during the measurements, the battery pack from the instrument was placed immediately behind the imager head so that it's lead-acid cell blocked this radiation.

Four images of this cask were obtained. The first was a 20-minute, wide-angle integration from 8.65 m with a pixel size of ~ 19.8 cm (Fig. 12.) Following this image, problems with the instrument required removing it for repair. For subsequent side-view measurements, the

imager was moved closer to the cask. The second integration comprised a total of 180 minutes from 6.14 m with a pixel size of ~ 8.5 cm (Fig. 13.) The third measurement was for a total of 120 minutes from the same distance but with a wider field of view resulting in pixels 14.1 cm across (Fig. 14.) Finally, a lift was used to obtain an oblique, top-down, view (Fig. 15.)

The overhead measurement provided several logistics challenges that might have affected the quality of the image. First, the imager had to be started with the lift retracted and then raised to the viewing position. This took varying times of order a few minutes. To change the mask to its anti-mask configuration, required lowering the imager, rotating the mask and re-raising the

Table 1
Cask Load Summaries

Cask	Type	Origin	Fuel Units	MTHM
1	MC-10	Turkey Point B-17	21	9.27
		Turkey Point	1	0.41
		VEPCO	12	5.31
			34	14.99
2	NuPac 125B	TMI Epoxy	2	0.02
3	GNS V/21	VEPCO	21	9.27
4	REA-2023	LOFT FP-1	1	0.20
		LOFT FP-2	2	0.10
		CT Yankee	1	0.39
		Dresden I	1	0.11
		Dresden I	1	0.06
		H.B. Robinson	1	.23
		Peach Bottom	2	.28
		LFRSB	1	0.31
		35 encaps. tubes	3	0.09
		Surry	1	0.02
			14	1.79
5	VSC-17	DRCT	17	5.31
6	TN-24P	DRCT	7	6.14
		LOFT Center	4	0.81
		LOFT Corner	4	0.28
		LOFT Std	4	0.81
			19	8.04

Table 2.
Cask Images

Cask		Gamma-Ray Images						Neutron Images					
Number	Type	View	Res (cm)	Range (m)	Exposure (min)	Counts/sec	Figs	View	Res (cm)	Range (m)	Exposure (min)	Counts	Figs
1	MC-10	Side wide	18.3, 19.8	8.65	20	1178	10	Side	64	8.1	360	4.5 x 10 ⁶	18, 20
		Side Wide	14.1, 13.1	6.14	180	1367	14						
		Side Zoom	13.1, 14.1	6.14	120	1325	13						
		Top	7.0, 6.5	3.0	160	513	15						
		Spectrum	--	3	16.7	--	17						
2	NuPac 125B	Spectrum	--	3	16.7	--	21	None					
3	GNS V/21	Side Wide	14.1, 13.1	6.15	60	396	22	Side	54	6.8	900 960	10 ⁷ 1.06 x 10 ⁷	24, 25
		Spectrum	--	3	16.6		23						
4	REA-2023	Side Wide	13.8, 12.8		60	962	26	Side	36	4.5	120	1.1 x 10 ⁶	28
		Spectrum	--	3	33.3	--	27						
5	VSC-17	Side Wide	17.8, 19.2	8.38	60	702	30	Side Hi-res	19	5.8	60	0.8 x 10 ⁶	33, 34
		Side Zoom	11.5, 10.6	8.38	50	675	31	Side Lo-res	46	5.8	120	1.7 x 10 ⁶	35
		Spectrum	--	3	16.6	--	32						
6	TN-24P	None						Side	53	6.8	60	0.5 x 10 ⁶	37
		Spectrum	--	3	16.6	--	36						

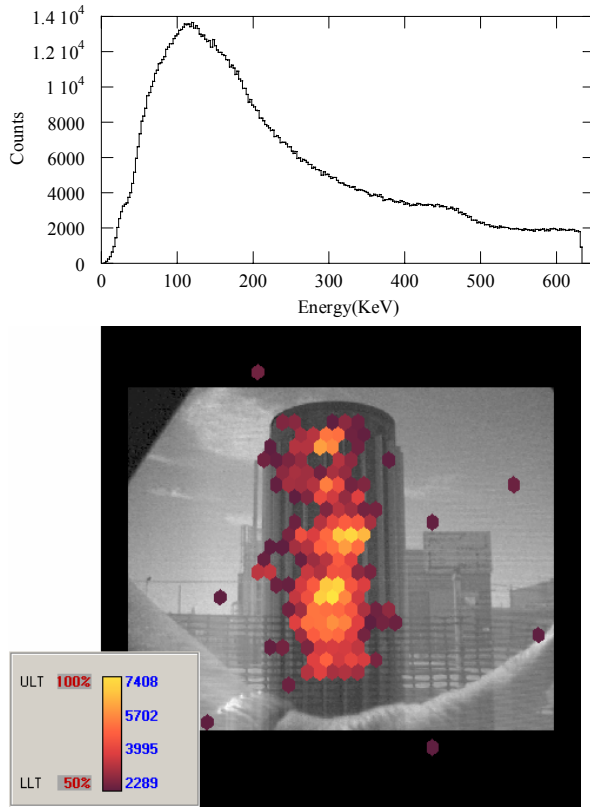


Fig. 12. First cask image (bottom) taken of cask 1 (MC-10) for a total integration time of 20 minutes. The pixels are ~ 19 cm in size. The associated spectrum is also given (top).

platform. As there was no precision control to the height, this was monitored by measuring the distance to the ground of the first scissor pivot-point (see Fig. 16.)

The overhead data was collected in two runs of 70 and 90 minutes from a distance to the cask center of 3 m. This provided a pixel size of ~ 7.0 cm. Note that the instrument was buffeted by the wind during the measurement. Lateral motions of ~ 3 cm were observed. The data shown in Fig. 15 comprises the full duration of the runs. Partial playback, omitting the first 10% of the data to compensate for different lift times, did not qualitatively affect the images.

Germanium Spectrometer Data

The spectrum obtained from Cask 1 is shown in Fig. 17. It represents 1000 sec of livetime with a deadtime fraction of 22.9%. The MC-10 spectrum shows prominent gamma-ray lines of the fission products ^{137}Cs , ^{60}Co and ^{154}Eu ; and contains boron, calcium, hydrogen, iron and silicon neutron induced gamma-ray peaks as well.

Neutron images

In order to avoid crowding of the instruments, the neutron imaging measurements were performed in a differ-

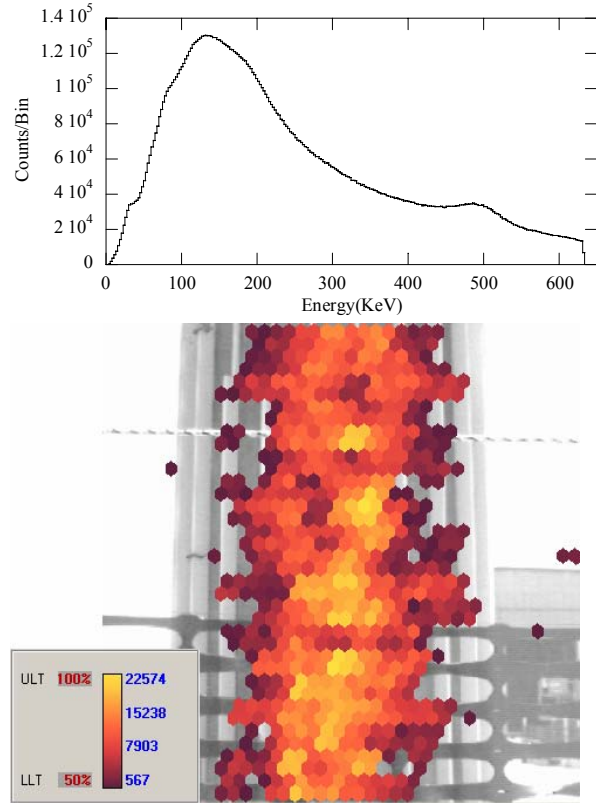


Fig. 13. Zoomed view of cask 1. The pixels are ~ 13.5 cm in size. The integration time was 3 hours.

ent sequence, but are reported here in the same cask order as the gamma imaging for comparison purposes. Cask MC-10 thermal neutrons were imaged last, from a distance of 8.12 m from the center of the cask with a 10-cm focal length, using the “A” mask (19×19 pixels). The field of view was 12.2 meters, and a pixel corresponds to 64 cm in the source plane. The count rate was about 250 neutrons per second. Independent exposures of 60 minutes and 120 minutes, each, were acquired with the mask in both the normal and anti-mask rotations. The six hours of data were combined into a single image to minimize the random statistical fluctuations. Fig. 18 shows the final image with unsmoothed data binned into areas corresponding to $\frac{1}{4}$ of the mask pixel area. It is not clear whether fluctuations in intensity on the scale of one pixel show any significant features in the fuel assembly, because the image still contains a lot of statistical noise. A histogram of the pixel intensities from the unsmoothed image is shown in Fig. 19. Note that only a small fraction of the pixels have intensities greater than 150, on a re-normalized scale of 0-255. These pixels represent the brightest and most significant regions of the image. However, they are still statistically noisy. Many of these fluctuations are minimized in the smoothed image (Fig. 20), which shows the entire cask glowing fairly uniformly.

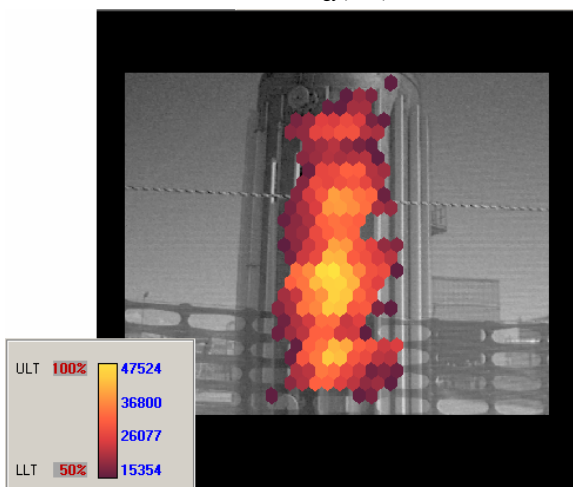
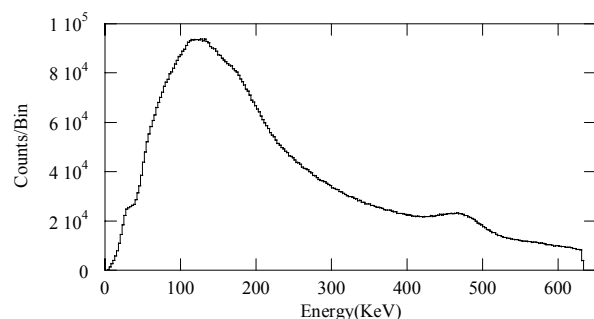


Fig. 14. Second wide-angle image of cask 1 and the associated spectrum. The pixels are ~ 14 cm in size. The integration time was 2 hours.

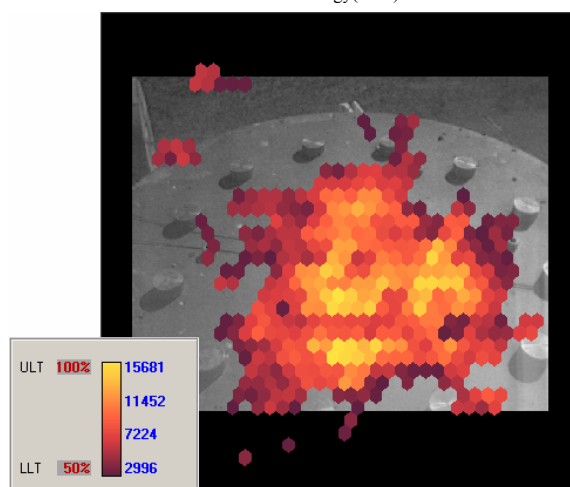
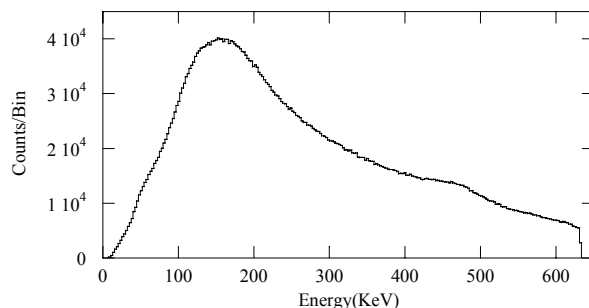


Fig. 15. Overhead view of Cask 1. The pixels are ~ 6.8 cm in size. The total integration time was 160 minutes. Note the difference in the spectrum between this view and that obtained from the side.

Cask 2: NuPac 125B

Gamma-ray images

No Gamma-ray images of this cask were obtained.

Ge Spectrometer

The spectrum obtained from Cask 2 is shown in Fig. 21. It represents 1000 sec of livetime with a deadtime fraction of 21.2%. The NP-125B spectrum shows prominent gamma-ray lines of the fission products ^{137}Cs , ^{60}Co , and ^{154}Eu ; and it contains boron, calcium, hydrogen, iron, and silicon neutron-induced gamma-ray peaks as well.

Neutron images

No neutron images of this cask were obtained.

Cask 3: GNS V/21

Gamma-ray images

Images of Cask 3, the Castor V/21, were obtained on the last day of measurements. The first two exposures were obtained from the south side of the pad. Both of these showed poor mask/anti-mask balance. This was traced to the make-shift cinderblock arrangement to shield the imager from the sun. In the early morning the relative sun motion required moving the sun-shield



Fig. 16. The lift used to take top-down images of Cask 1.

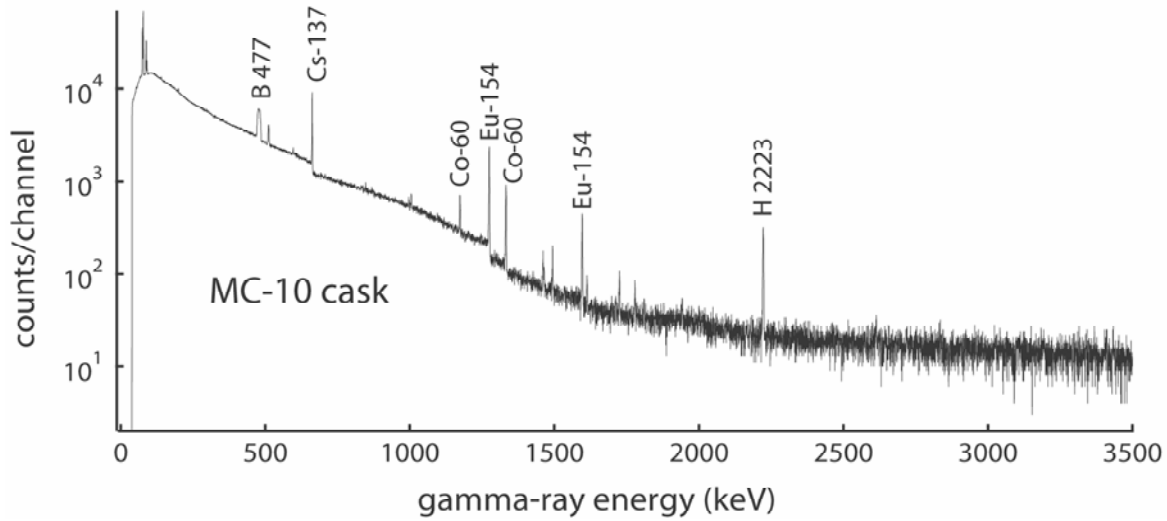


Fig. 17. High resolution spectrum of Cask 1.

more frequently and to a greater extent. Unfortunately, this also meant moving the cinderblock used to keep the contrivance from blowing away in the wind. In moving the cinderblock, we changed the shielding configuration of the system and unbalanced the mask/anti-mask integrations.

A second attempt to image Cask 3 was performed from the North side. This resulted in the image in Fig. 22. The pixel size in the image is ~ 13.6 cm. Note that the image was very noisy so that the gamma-ray threshold is set to 60% of the maximum level rather than the 50% used in other images. The morphology of the image is consistent with radiation coming out the bottom of the cask and scattering off of the ground. It is not clear why the contrast is so poor in the image. The number of

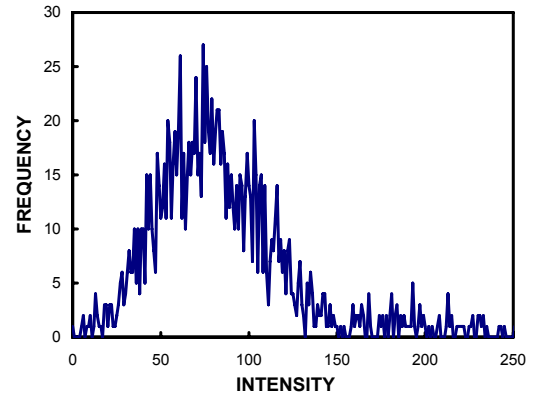


Fig. 19. Histogram of pixel intensities from data in the unsmoothed image.

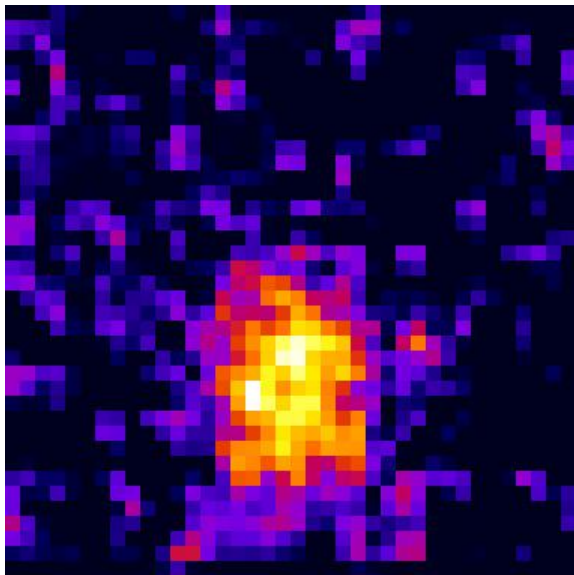


Fig. 18. Thermal-neutron image of cask MC-10 processed in bins equal to $\frac{1}{4}$ of a mask pixel area.

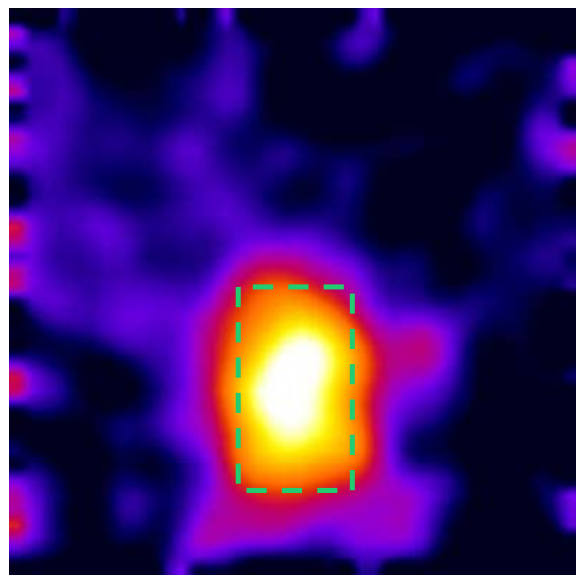


Fig. 20. Smoothed neutron image of cask 1 with the green rectangle indicating the size of the cask

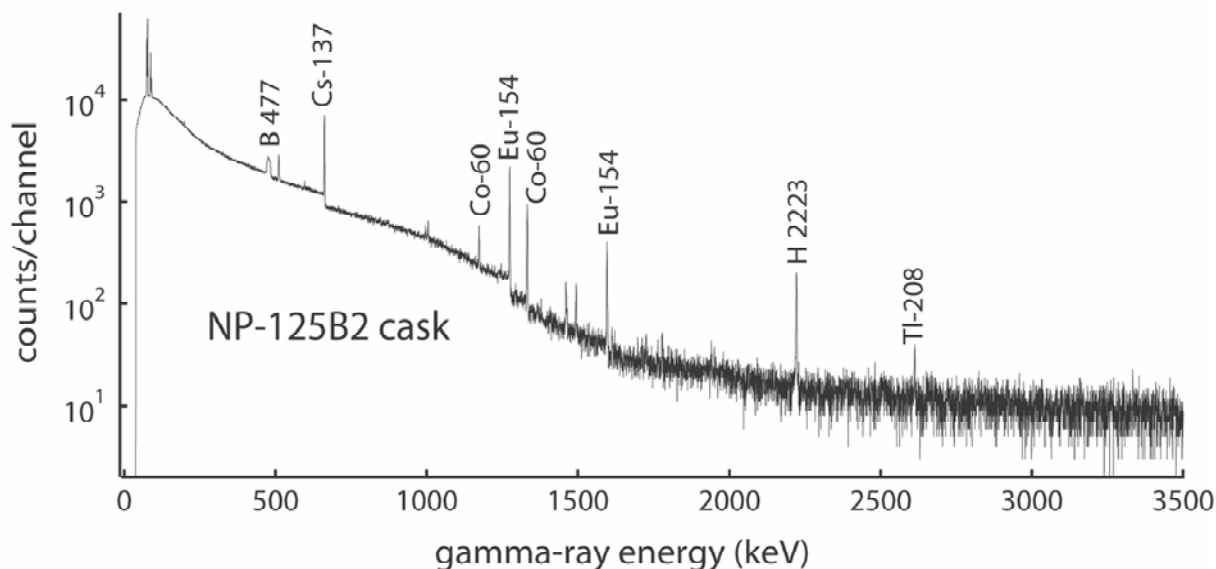


Fig. 21. Spectrum of Cask 2.

events in the image is 3.46×10^6 , a number commensurate with other higher-contrast images. Unfortunately, a background rate at the location was not obtained. It is possible that the neighboring casks produced a large

fraction of the counts from radiation that penetrated the 0.95 cm thick Pb shielding around the detector. This amounts to ~ 0.8 mean free paths at 662 keV.

Germanium Spectrometer Data

The spectrum obtained from Cask 3 is shown in Fig. 23. It represents 1000 sec of livetime with a deadtime fraction of 21.2%. The V/21 spectrum shows prominent gamma-ray lines of the fission products ^{137}Cs , ^{60}Co , and ^{154}Eu ; and it contains boron and hydrogen neutron-induced gamma-ray peaks as well.

Neutron image

Cask 3 was imaged with the “A” mask in the normal position over an acquisition period of 15 hours. The resulting smoothed image, shown in Fig. 24, suggests a dark vertical band in the center of the image, with brighter regions at the edges. The contrast is weak, and could be affected by imaging artifacts, but at face value it indicates that the cask is heavily shielded for thermal neutron leakage, so that it looks darker than the surrounding background of neutrons scattered in the atmosphere. A 1-hour antimask image was also acquired, but those data contained more statistical noise than the overnight run and, after scaling the data appropriately, the combined mask-antimask image was washed out (Fig. 25.) Clearly, the mask and antimask data should be acquired for the same time for optimal results.

Cask 4: REA-2023

Gamma-ray images

The gamma-ray image of cask 4 was obtained from the north side of the pad at a distance of 6.0 m. A single wide-field image (see Fig. 26) was obtained in 60 minutes total integration time. The approximate resolution is 13.5 cm per pixel. A total of 3.46×10^6 counts were

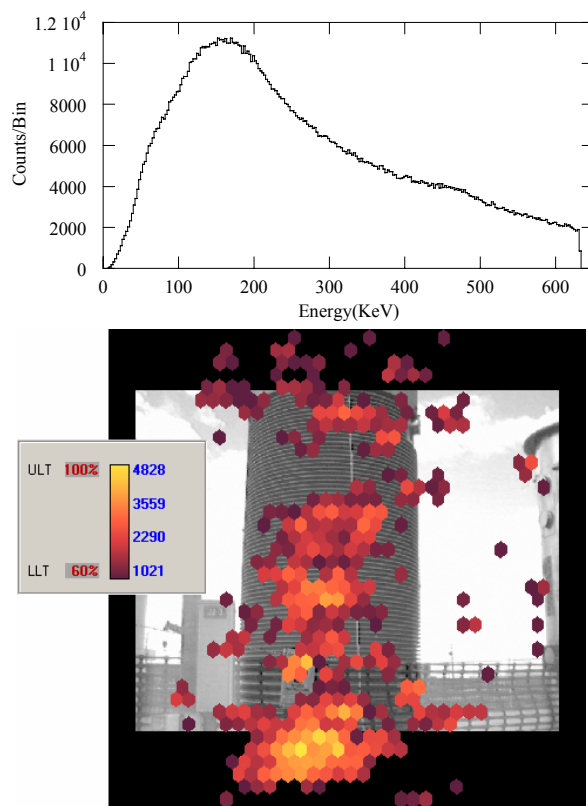


Fig. 22. Wide-field Image of Cask 3. The gamma-ray threshold in this image is set to 60% of the maximum intensity. The pixel size is ~ 13.6 cm and the integration time was one hour.

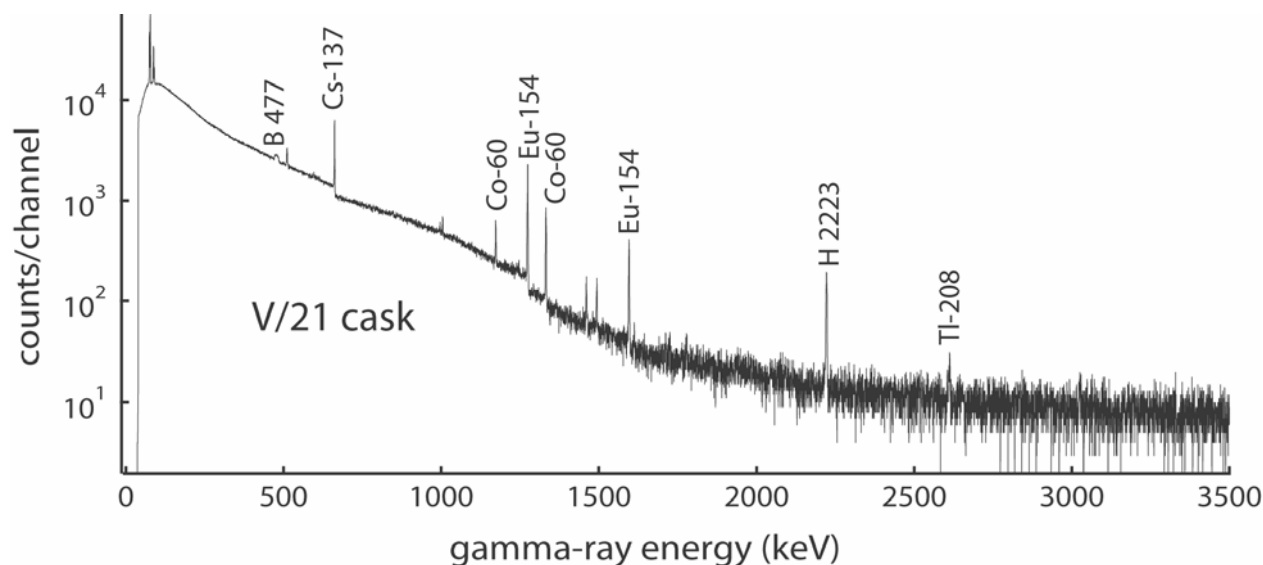


Fig. 23. Spectrum from Cask 3.

recorded by the imager. The image clearly shows that the radiation is confined to the central region of the cask and is uniform along its length. However, the contrast in the image is relatively low.

Germanium Spectrometer Data

The spectrum obtained from Cask 4 is shown in Fig. 27. It represents 1000 sec of livetime with a deadtime fraction of 22.9%. The REA-2023 spectrum shows prominent gamma-ray lines of the fission products, ^{137}Cs , ^{60}Co , and ^{154}Eu ; and it contains boron, hydrogen, and iron neutron-induced gamma-ray peaks as well.

Neutron image

The combined mask-anti-mask image obtained for cask 4 is shown in Fig. 28 after smoothing and contrast enhancement. The bright vertical stripe in the middle of the image is much narrower than the exterior dimensions of the cask (shown in green dashes.) This appearance may be somewhat exaggerated by the thresholding effect of the false colors, but is consistent with the gamma-ray image in Fig 26, which is also narrow. A horizontal profile of the neutron intensity (see Fig. 29) does not show a sharp edge for the bright region, but is slightly more peaked than a cosine distribution that one might expect for transmission through an annular absorber.

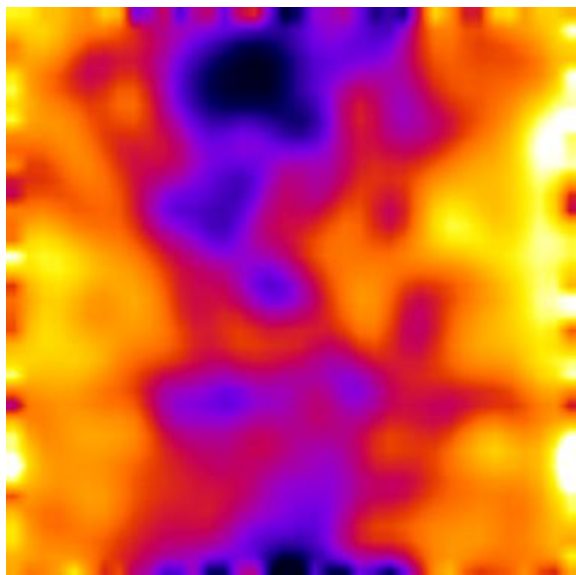


Fig.24. Smoothed, 15-hr, neutron image of cask 3 with mask-only data. The cask emits a lower flux of neutrons than from the surrounding area.

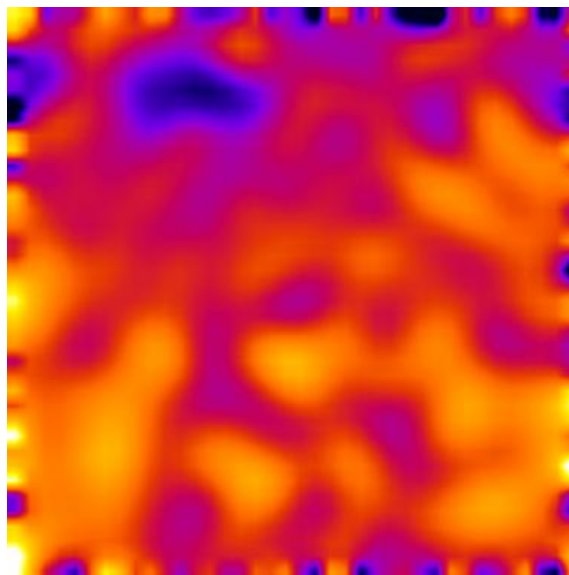


Fig. 25. Smoothed neutron image of Cask 3 after subtracting 1-hr anti-mask data having poorer statistics than the overnight run.

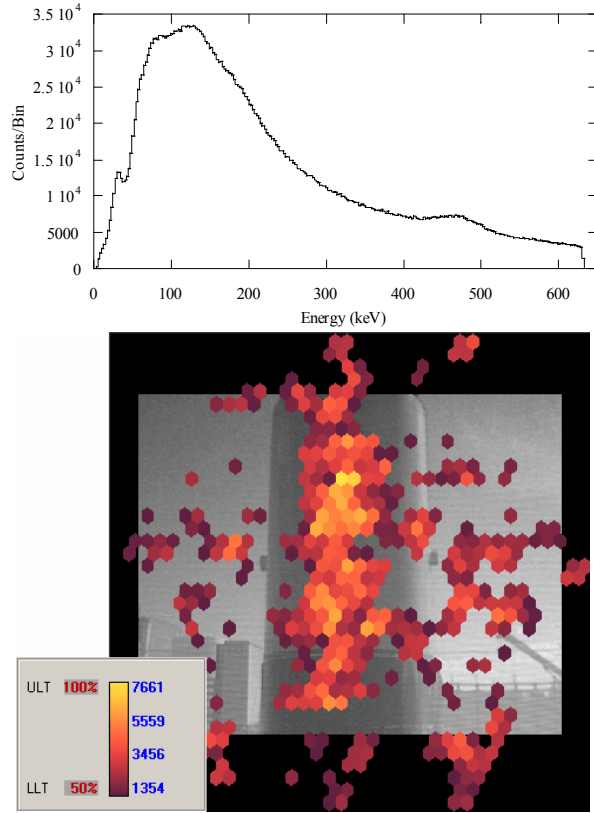


Fig. 26. Wide-angle image of cask 4 and the associated spectrum. The pixel size is ~ 13.5 cm and the integration time was 1 hour.

Cask 5: VSC-17

Gamma-ray images

Two images of cask 5, the Pacific Sierra Nuclear VSC-17, were obtained. Both were obtained from a distance of 8.38 m. The first was a wide-angle image with a total exposure time of one hour and a pixel size of ~ 18.5 cm. It is shown in Fig. 30. A zoomed image with an

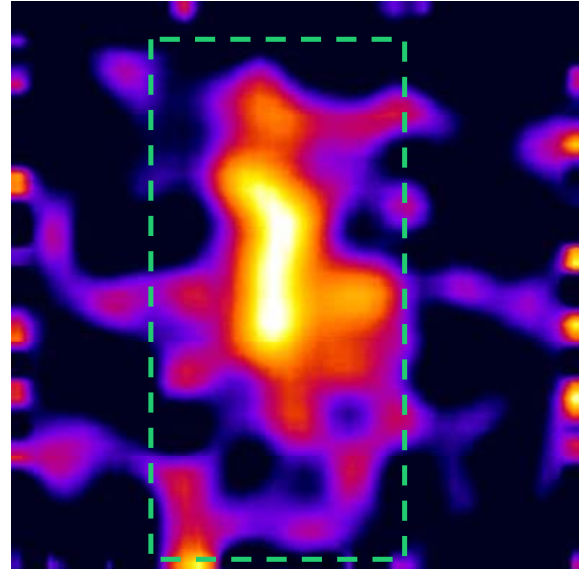


Fig. 28. Smoothed mask-antimask neutron image of cask 4.

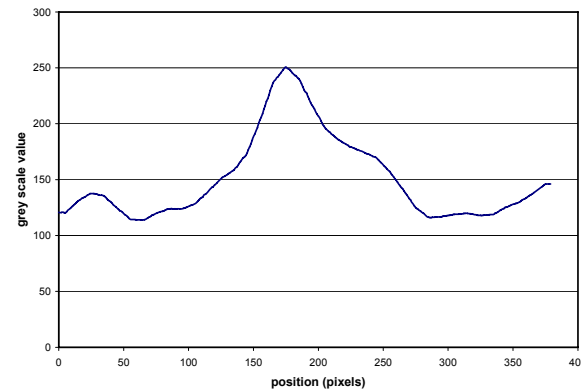


Fig. 29. Intensity profile across the image of cask 4.

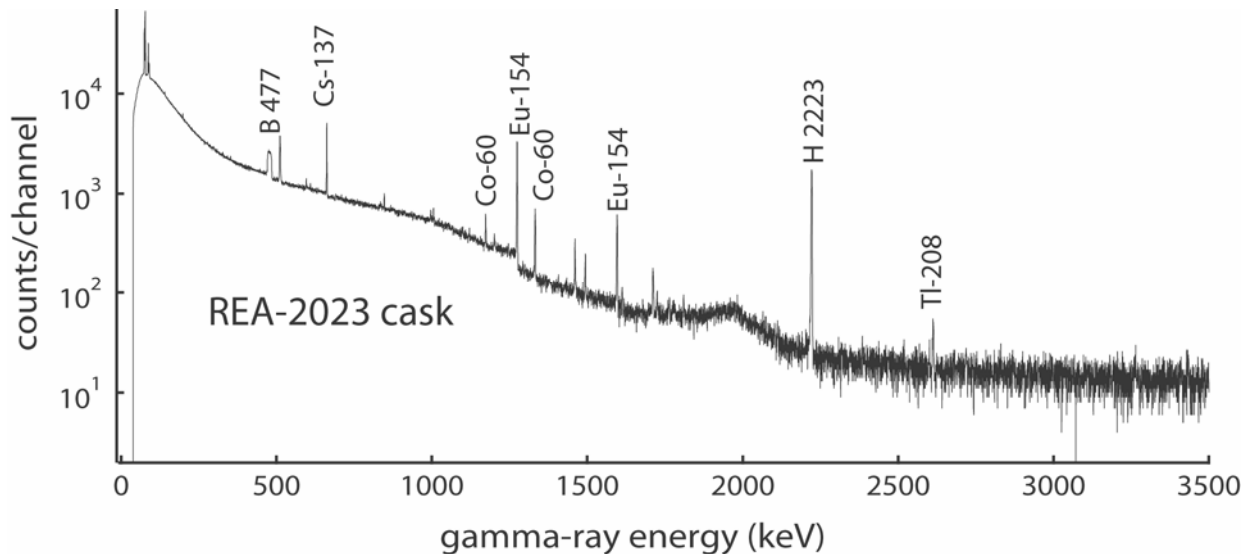


Fig. 27. Spectrum obtained from cask 4. Note that this is for 2000 sec. livetime, twice that of the other spectra.

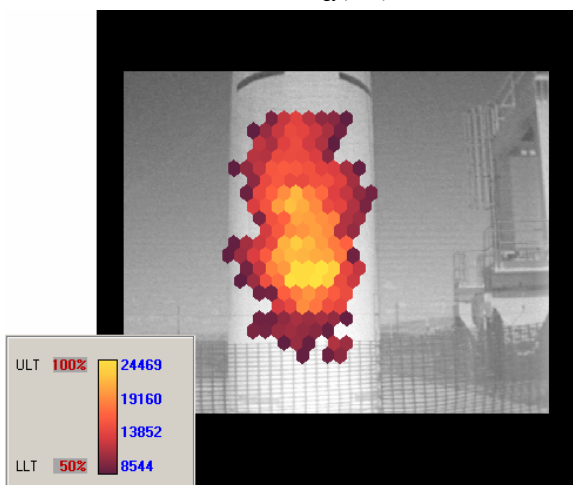
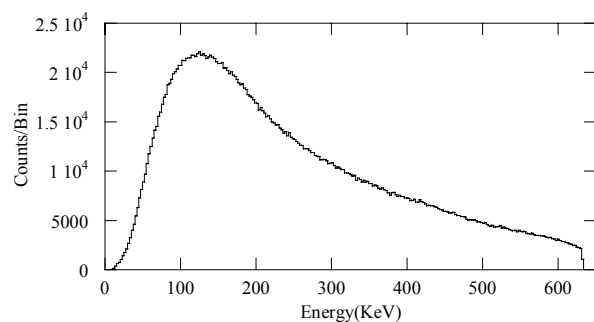


Fig. 30. Wide-angle image of cask 5 and the associated spectrum. The pixel size is ~ 18.5 cm and the integration time was 1 hour.

average pixel size of 11 cm is shown in Fig. 31. This data represents 43 min. out of the total 60 min. integration. The imager was bumped during the last 10 minutes of the anti-mask run. Consequently only the first 71% of each file was replayed to obtain the image shown. The gamma-ray images clearly show a bright region that is centered on the cask horizontally and it appears hotter near the bottom of the cask.

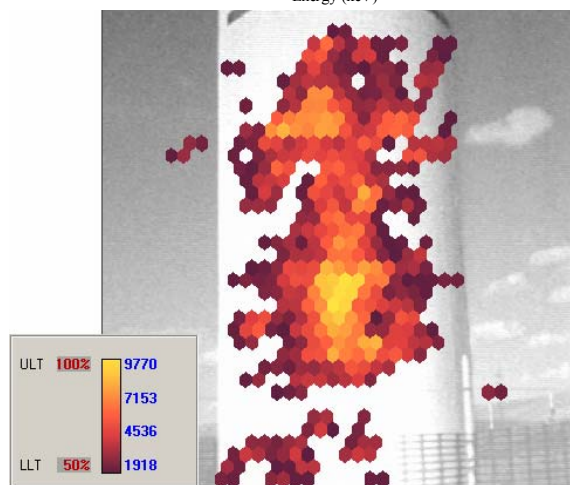
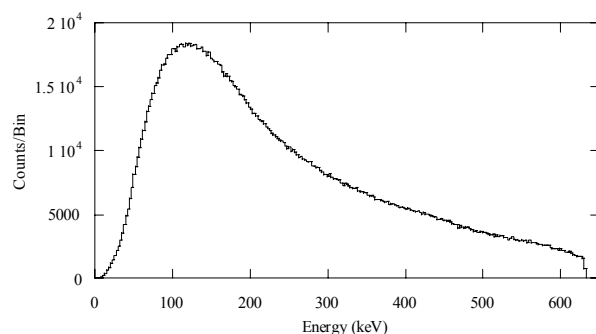


Fig. 31. Zoomed view of Cask 5. The pixel size is ~ 11 cm and the integration time was 43 minutes.

Spectrometer Data

The spectrum obtained from Cask 5 is shown in Fig. 32. It represents 1000 sec of livetime with a deadtime fraction of 26.1%. The VSC-17 spectrum shows prominent gamma-ray lines of the fission products ^{137}Cs , ^{60}Co , and ^{154}Eu ; and it contains calcium, hydrogen, iron, and silicon neutron-induced gamma-ray peaks as well.

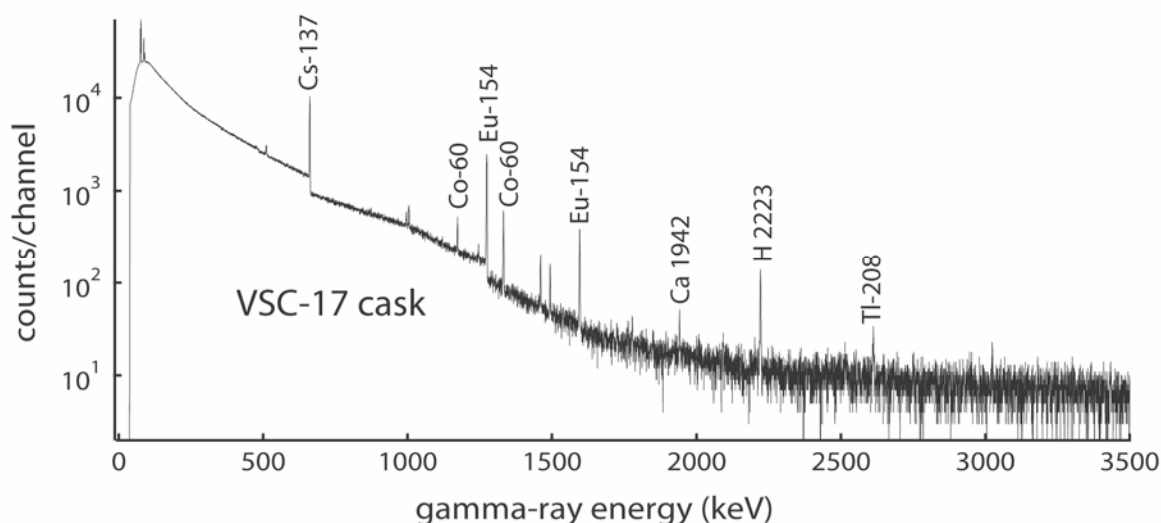


Fig.32. Energy spectrum from cask 5.

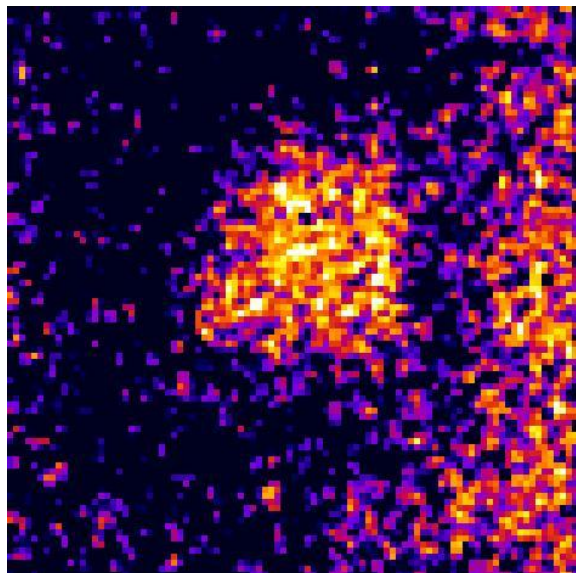


Fig. 33. Neutron image of cask 5 using 47 x 47 pixel mask, binned into areas corresponding to $\frac{1}{4}$ of a mask pixel.

Neutron image

The image in Fig. 33 was an attempt to obtain the best spatial resolution with mask “C”. One consequence of choosing small pixels is that the counts in each pixel become smaller relative to the statistical uncertainty derived from the total number of counts in the image. Subsequent smoothing can improve the image quality, as shown in Fig. 34, but long exposures are necessary before the smaller features in such images are considered significant.

In these two images, a bright region is seen at the right side of the picture, possibly due to partially encoded neutron flux coming from outside the primary field of view. In subsequent mask-antimask images acquired from the same position using lower resolution, this artifact was eliminated (Fig. 35.)

Cask 6: TN-24P

Gamma-ray images

No gamma-ray images of this cask were obtained.

Ge spectrometer

The spectrum obtained from cask 6 is shown in Fig 36. It represents 1000 seconds of livetime with a deadtime fraction of 18.7%. The TN-24P spectrum shows prominent gamma-ray lines of the fission products ^{137}Cs , ^{60}Co , and ^{154}Eu ; and it displays calcium, hydrogen, and silicon neutron-induced gamma-ray peaks as well.

Neutron image

Cask 6 was the first one to be imaged with the neutron camera, and attempts were made both with the “C” and

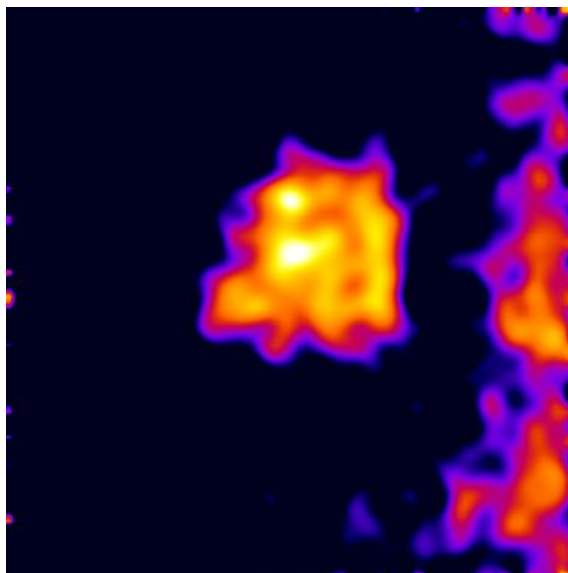


Fig. 34. Smoothed and thresholded neutron image of cask 5 using “C” mask.

“A” masks. In neither case was an interesting or meaningful shape discerned in the images (see Fig. 37.) This cask appears to emit relatively few thermal neutrons.

Discussion

The primary goal of the project was to determine if cask fingerprinting is a viable technique. To this end, the images obtained with the two systems clearly demonstrate the proof-of-principle that the radiation fields emitted by the casks can be imaged. They also demonstrate that the fields are different depending on the cask

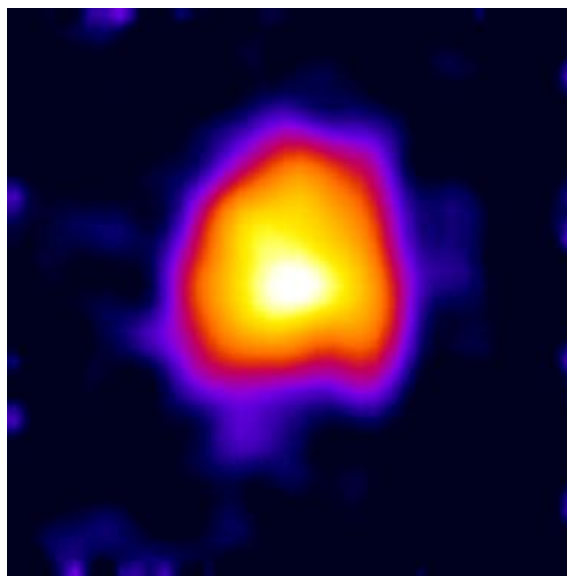


Fig. 35. Mask-antimask image of cask 5 using 19 x 19 pixel mask, with smoothing and thresholding.

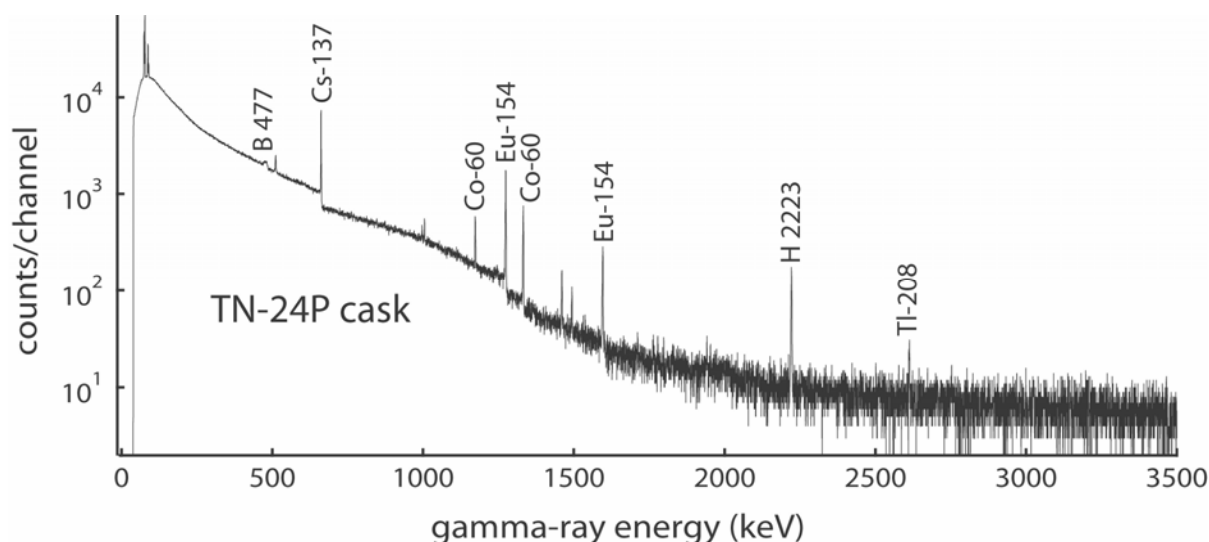


Fig.36. Energy spectrum from cask 6.

type.

Gamma-Ray Results

In Fig. 38 we provide a side-by-side comparison of the wide-field, whole-cask images obtained with the gamma-ray imager. To the right and below each of the false-color images is a histogram of the counts per pixel for the pixels that fall under the yellow cursor lines in the main image. These plots can be used to obtain a better idea of the signal-to-noise ratio and provide further information on the overall shape of the images. From the figure, it is clear that the overall morphology of the radiation fields vary significantly. For instance casks 1 and 5 provide intense radiation from the central regions of the cask while casks 3 and 4 have relatively

poor contrast. The image of cask 3 is suggestive of fuel being stored at the very bottom of the cask. This pattern is actually attributed to radiation leakage from the poorly shielded cask bottom and its subsequent scatter into the line of sight of the gamma-ray imager.

In fact, it would appear that scattered radiation dominates all of the images obtained with the gamma-ray imager. This is not surprising given that one of the primary cask functions is to shield the surroundings from the radiation emitted by the cask contents. As mentioned in the introduction, one expects the observed radiation pattern to have both a scattered and an unscattered component. One also expects that these two images should be separable based on energy cuts. This concept is validated by the data from the germanium spectrometer that clearly shows photopeaks are detected in the gamma-ray flux.

The spectral data is summarized in Table 3. The numerical analysis shows that some of these peaks have excellent signal-to-noise ratios. Hence an image made of the line-radiation should provide clear images of the fuel assemblies. Unfortunately, the peaks are all above the useful energy range of the current imager. This shortcoming arises from the use of an extant imager to undertake the measurements and is not a fundamental limitation of the imaging techniques.

When taken together, the spectrometer data and the gamma-ray images obtained, show significant promise that the fingerprinting technique can be used. Most of the images are just what one would expect for the scattered component of the gamma-ray field. The images show the overall location of the sources, but with all detail washed out by the scattering process. Hence, the top view of cask 1 (Fig. 15) shows the elliptical shape

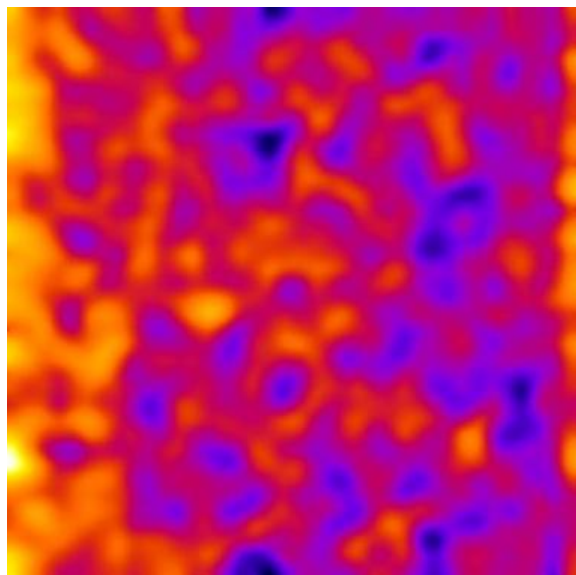


Fig. 37. Neutron image data from cask 6. This cask appeared to be weak in thermal neutron output.

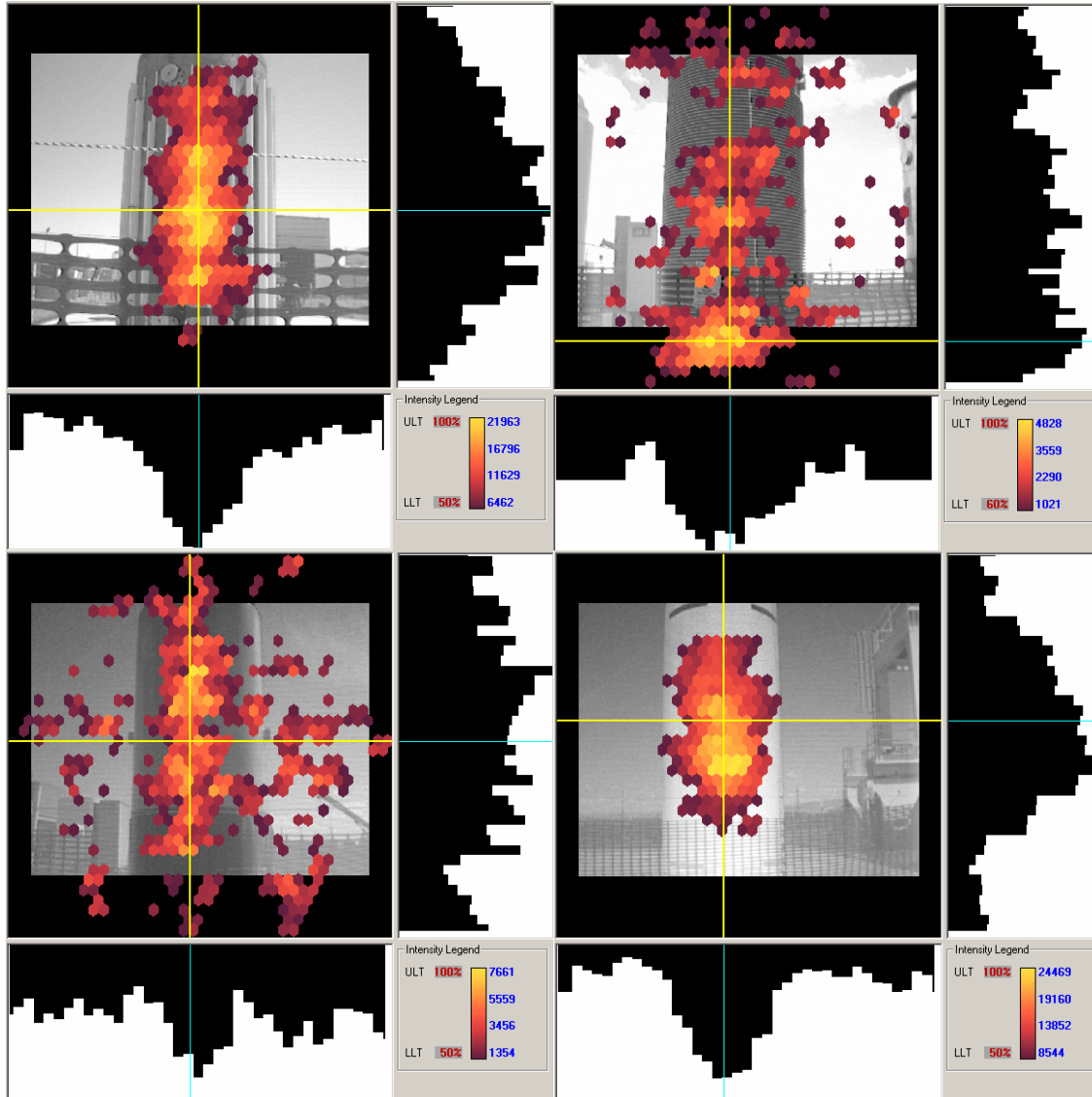


Fig. 38. Wide-field, gamma-ray images of casks (clockwise from top left) 1, 3, 4 and 5. The exposures are from similar distances and one hour in duration. The histograms on the right and bottom of the individual images are the counts under the vertical and horizontal cursor lines, respectively.

appropriate for a projection of the circular source distribution one would expect, while the side view shows the appropriate rectangular projection. Unfortunately, it is clear from the images obtained that insufficient detail exists to achieve the end-goal of individual cask identification.

To realize a successful fingerprint will require increasing the level of detail in the images. At a minimum, one will require the ability to image the individual fuel assemblies loaded around the periphery of the cask. Our results show that this means creating an image using primarily non-scattered radiation. Since gamma-rays lose energy when they scatter, any radiation detected in

a nuclear emission line cannot have scattered on the way out of the cask and should carry the fingerprint information desired. The data from the Ge spectrometer, clearly shows that significant line emissions survive to the cask surface. If we look at the 662 keV line from the various casks, we find that the ratio of unscattered to scattered radiation varies from $\sim 0.54:1$ for cask 3 to $1.24:1$ for cask 5. However, an examination of the spectrum for the best case shows that for a NaI-type energy resolution, this degrades by approximately a factor of 20 to $0.06:1$. This degradation is primarily due to the large scattered component created in the lines and indicates that an instrument with good spectral resolution is required.

Table 3
Summary of Spectroscopic Measurements

cask	type	gamma-ray			Counts				Significance		remarks
		nuclide	energy, keV	type	gross	net	sigma	bkg	Net/sigma	net/bkg	
1	MC10	B	477	capture	105732	2297	543	103435	4.2	0.022	
	1000 live sec 22.9% dead	Cs-137	662	fiss. prod.	62420	30231	348	32189	86.9	0.939	
		Co-60	1173	fiss. prod.	6864	1906	104	4958	18.3	0.384	
		Co-60	1332	fiss. prod.	6840	4214	107	2626	39.4	1.605	
		Eu-154	1274	fiss. prod.	16038	11070	168	4968	65.9	2.228	
		Eu-154	1596	fiss. prod.	3355	2134	77	1221	27.7	1.748	
		Fe	1725	capture	1167	336	51	831	6.6	0.404	
		Si	1778	(n, n' gamma)	751	216	31	535	7.0	0.404	
		Ca	1942	capture	489	47	20	442	2.4	0.106	
		H	2223	capture	2591	1947	64	644	30.4	3.023	
		Si	3536	capture	312	56	26	256	2.2	0.219	
2	125B2	B	477	capture	29452	298	156	29154	1.9	0.010	
	1000 live sec 16.1% dead	Cs-137	662	fiss. prod.	42340	22396	256	19944	87.5	1.123	
		Co-60	1173	fiss. prod.	7871	1996	143	5875	14.0	0.340	
		Co-60	1332	fiss. prod.	6921	4432	114	2489	38.9	1.781	
		Eu-154	1274	fiss. prod.	13460	10061	136	3399	74.0	2.960	
		Eu-154	1596	fiss. prod.	2977	1962	76	1015	25.8	1.933	
		Fe	1725	capture	540	107	27	433	4.0	0.247	
		Si	1778	(n, n' gamma)	569	172	29	397	5.9	0.433	
		Ca	1942	capture	535	62	35	473	1.8	0.131	
		H	2223	capture	1669	1129	54	540	20.9	2.091	
		Si	3536	capture	196	36	14	160	2.6	0.225	

cask	type	gamma-ray			Counts				Significance		remarks
		nuclide	energy, keV	type	gross	net	sigma	bkg	Net/sigma	net/bkg	
3	V/21	B	477	capture	99121	5611	687	93510	8.2	0.060	
	1000 live sec 21.2% dead	Cs-137	662	fiss. prod.	52646	19112	369	33534	51.8	0.570	
		Co-60	1173	fiss. prod.	7307	1691	132	5616	12.8	0.301	
		Co-60	1332	fiss. prod.	6725	3820	122	2905	31.3	1.315	
		Eu-154	1274	fiss. prod.	14452	10875	144	3577	75.5	3.040	
		Eu-154	1596	fiss. prod.	2897	2039	64	858	31.9	2.376	
		Fe	1725	capture							not observed
		Si	1778	(n, n' gamma)	506	56	27	450	2.1	0.124	
		Ca	1942	capture							not observed
		H	2223	capture	1704	1275	51	429	25.0	2.972	
		Si	3536	capture							not observed
4	REA-2023	B	477	capture	63015	1467	487	61548	3.0	0.024	
	2,000 live sec 9.3% dead	Cs-137	662	fiss. prod.	33575	14724	235	18851	62.7	0.781	
		Co-60	1173	fiss. prod.	7215	1388	118	5827	11.8	0.238	
		Co-60	1332	fiss. prod.	6482	3009	113	3473	26.6	0.866	
		Eu-154	1274	fiss. prod.	22251	15607	208	6644	75.0	2.349	
		Eu-154	1596	fiss. prod.	4927	3041	91	1886	33.4	1.612	
		Fe	1725	capture	1287	185	46	1102	4.0	0.168	
		Si	1778	(n, n' gamma)							not observed
		Ca	1942	capture							not observed
		H	2223	capture	12483	11522	124	961	92.9	11.990	
		Si	3536	capture							not observed

		gamma-ray			Counts				Significance		
cask	type	nuclide	energy, keV	type	gross	net	sigma	bkg	Net/sigma	net/bkg	remarks
5	TN-24P	B	477	capture	87396	5664	704	81732	8.0	0.069	
	1000 live sec 18.7% dead	Cs-137	662	fiss. prod.	45640	25308	287	20332	88.2	1.245	
		Co-60	1173	fiss. prod.	6051	1712	118	4339	14.5	0.395	
		Co-60	1332	fiss. prod.	5139	3410	94	1729	36.3	1.972	
		Eu-154	1274	fiss. prod.	11153	8205	138	2948	59.5	2.783	
		Eu-154	1596	fiss. prod.	2399	1414	76	985	18.6	1.436	
		Fe	1725	capture							not observed
		Si	1778	(n, n' gamma)	284	63	17	221	3.7	0.285	
		Ca	1942	capture	329	40	23	289	1.7	0.138	
		H	2223	capture	1173	889	41	284	21.7	3.130	
		Si	3536	capture	150	7	11	143	0.6	0.049	
6	VSC-17	B	477	capture				0			not observed
	1000 live sec, 26.1% dead	Cs-137	662	fiss. prod.	69212	35306	406	33906	87.0	1.041	
		Co-60	1173	fiss. prod.	6025	1398	113	4627	12.4	0.302	
		Co-60	1332	fiss. prod.	4455	2481	86	1974	28.8	1.257	
		Eu-154	1274	fiss. prod.	15571	11935	157	3636	76.0	3.282	
		Eu-154	1596	fiss. prod.	2956	2042	72	914	28.4	2.234	
		Fe	1725	capture	549	76	35	473	2.2	0.161	
		Si	1778	(n, n' gamma)	429	71	24	358	3.0	0.198	
		Ca	1942	capture	368	108	20	260	5.4	0.415	
		H	2223	capture	1024	695	38	329	18.3	2.112	
		Si	3536	capture	92	19	10	73	1.9	0.260	

Ideal Gamma-Ray Imager

The results obtained during the measurement campaign provide some design parameters for a gamma-ray imager that should be able to obtain unique cask fingerprints. As discussed above, the spectral resolution will have to be high to obtain a useable signal to noise ratio. In addition, the flux in the line radiation indicates a detector surface area of $\sim 50 \text{ cm}^2$ will provide reasonable images on hour timescales.

Ideally the field of view would encompass the entire cask with enough resolution to isolate individual fuel rod assemblies. With typical 2 m x 5 m cask dimensions and a fuel assembly center-to-center spacing of $\sim 20 \text{ cm}$, a minimum of ~ 20 , 10-cm pixels are required across the cask, with 2.5 times that number to see the full cask height. This gives a field of view with $\sim 50 \times 50$ resolution elements. To properly oversample such a mask pattern requires a detector with $\sim 100 \times 100$ pixels. For an end-on-view, only half this number would be required in each dimension.

With the high fill factor of the gamma-ray emitting surfaces, the optimum signal-to-noise performance will occur with a coded aperture imager having less than a 50% open fraction.[4] In fact, for a system taking end views, a pin-hole camera may be able to obtain images in almost the same time as a coded aperture imager. It has a further advantage that concerns of seeing neighboring casks with a partially coded pattern are not present. This effect takes sources just outside the field of view and makes them appear on the opposite side of the image and increases systematic noise in the image. It can be removed with the simple design modification that incorporates collimation to restrict the field of view of every detector pixel to $\frac{1}{4}$ of the overall mask (a single mask pattern.) This will diminish the instruments sensitivity towards the edges of the field of view. The potential advantages of the pin-hole camera may be negated by the instrument weight since significant shielding will be required in the high-flux environment of a cask farm.

Because, the primary information content in the gamma-ray images comes from radiation at 662 keV and above, Compton imagers may prove a suitable imager type for this application. In these instruments the direction of origin of individual gamma-rays is localized to a ring of possible directions with the final image comprised of overlapping rings. The increased information obtained about each gamma-ray (a narrow ring, rather than $\frac{1}{2}$ to $\frac{1}{3}$ the field of view, as in a coded-aperture imager) means that signal to noise is improved. A number of groups are actively working on this technology,[16-18] but it will still be at least five years before practical instruments can be available.

Even then, the cost of such units is likely to be high ($\sim \$1\text{M.}$)

Neutron results

The creation of a meaningful cask image using thermal neutrons depends on three factors. First, there must be sufficient residual neutron activity from spontaneous fission or (α, n) reactions in the spent fuel assemblies. Second, a fraction of these fast neutrons must be thermalized by scattering with hydrogen before reaching the surface of the cask. Third, the thermal neutrons must be able to escape into the air by diffusion to the surface without being absorbed.

The casks constructed with an external concrete shell are most suitable to meet these requirements, provided they contain a sufficient quantity of neutron-producing spent-fuel materials. The fast neutrons have a mean free path in concrete which varies with the hydrogen content, but there is likely to be a measurable flux of thermal neutrons leaking from the surface. The multiple scattering of neutrons in thick concrete walls makes it difficult to extract much information about the shape of the fuel loading because the images are dominated by thermal neutrons diffusing to the external surfaces. However, there are still noticeable differences in shapes of the images obtained from casks 1, 2 and 5. These shapes provide a crude type of signature that is not easily predicted or faked.

Casks that are constructed predominantly of steel may be penetrated by significant fluxes of fast neutrons without much thermalization. Casks in which neutron absorbing layers like borated hydrocarbons are part of the design are unlikely to give a usable thermal neutron signature.

Just as with gamma-rays, there may be an unscattered component to the neutron flux. This would be carried by fast neutrons. In fact, the lack of an image of one of the steel casks was somewhat surprising at first, considering the neutron dose information taken by health physicists at the site. The cask with the highest dose provided no thermal-neutron signature. Since the dose meters rely on a thermalizing sphere of polyethylene to moderate the fast neutrons, the lack of a thermal-neutron image is a direct confirmation that fast neutrons are emitted by this cask. Thus, if a fast-neutron imager could be developed, it would probably be much more effective in characterizing the contents of the casks than thermal neutrons. A design for such an instrument is being developed by our BNL collaborators, and has shown promising results.

Conclusions

The results of the measurement campaign did not directly validate the concept of fingerprinting dry storage casks. However, they do suggest that further measurements are warranted. The gamma-ray results indicate that a significant flux of unscattered radiation does escape the casks. Further, they show that the signal-to-noise ratio is high enough to generate images if an imager with suitable high-energy response and energy resolution is used. The thermal-neutron results are less promising. However, there is evidence that fission-spectrum neutrons do reach the cask surface. If imaged, these neutrons should also provide unique cask signatures.

Recommendations

To determine if radiation signatures can be used to uniquely identify dry storage casks, further work is required. An additional measurement campaign should be conducted with a germanium-based or comparable gamma-ray imager. The two primary requirements for the follow-on instrument are extended energy response to fission product gamma-ray lines and neutron capture peaks, and excellent energy resolution (comparable to a Ge spectrometer.) Pending results from these measurements, a design study of the optimum imager for the cask farm environment should be undertaken. Additional measurements with a fission spectrum neutron imager are also clearly indicated. As such instruments are currently under development, the potential applications to the IAEA should be made known to the sponsoring agencies. As early as practical, a further measurement campaign with such an instrument should be conducted.

It is clear that the radiation levels from the fuel assemblies are sufficient to generate images, even through the heavy shielding in the cask walls. If unshielded, it should be possible to obtain gamma-ray images, even from significant distances. As such, an additional use for the imaging technologies would be to monitor loading of the casks. Given the intense radiation fields, it is possible that one could even obtain images in the short exposure times required to make motion pictures. The value of tracking the individual radioactive elements throughout the loading process should be considered by the safeguards community.

Acknowledgements

This work was performed under the auspices of the U.S. Department of Energy by University of California, Lawrence Livermore National Laboratory under Contract W-7405-Eng-48.

References

1. "Forming images with thermal neutrons", P.E. Vanier, L. Forman, Proc. SPIE, **4784A**, pp. 183-193, 2002.
2. *A Large-Area PSPMT Based Gamma-ray Imager with Edge Reclamation*, K.P. Ziock, L. Nakae, IEEE Trans. Nucl. Sci., **49**, 1552-1559, 2002.
3. *Coded aperture imaging with uniformly redundant arrays*, E.E. Fenimore, T.M. Cannon, Applied Optics, **17**, no. 3, pp. 337-347, Feb., 1978.
4. *Coded aperture imaging: predicted performance of uniformly redundant arrays*, E.E. Fenimore, Applied Optics, **17**, no. 22, pp. 3562-3570, Nov., 1978.
5. *Coded aperture imaging in X- and gamma-ray astronomy*, E. Caroli, J.B. Stephen, G. Di Cocco, L. Natalucci, A. Spizzichino, Space Sci. Rev., **45**, 394-403, 1987.
6. *A Gamma-Ray Imager for Arms Control Verification*, K.P. Ziock, T.B. Gosnell, C.J. Hailey, J.H. Lupton, F.A. Harrison, IEEE Trans. Nucl. Sci. **39**, 1046 (1992).
7. W. R. Cook, M. Finger, T.A. Prince, E.C. Stone, IEEE Trans. Nucl. Sci., **NS-31**, 771 (1984).
8. *New family of binary arrays for coded aperture imaging*, S. Gottesman, E. Fenimore, Applied Optics, **28**, no. 20, pp. 4344-4352, Oct. 1989.
9. Hamamatsu Photonics K.K., 314-5, Shimokanzo, Toyooka-village, Iwata-gun, Shizuoka-ken, 438-0193, Japan
10. *Real time generation of images with pixel-by-pixel spectra for a coded aperture imager with high spectral resolution*, K.P. Ziock, M.T. Burks, W. Craig, L. Fabris, E.L. Hull, N.W. Madden, NIM B, **505**, 420-424, 2003.
11. *Improvements in coded aperture thermal neutron imaging*, Peter E. Vanier, Proc. SPIE, **5199-A**, pp.124-131, 2003.
12. A.J. Caffrey, et al., IEEE Trans. Nuc. Sci. **39**, pp. 1422-1426, 1992.
13. *INEEL Spent Nuclear Fuel Integrated Transfer Schedule*, available from:

<http://www.id.doe.gov/DOEID/RFPSharedLibrary/refdoc.htm> as:

<http://www.id.doe.gov/DOEID/RFPSharedLibrary/PDF/PLN%20845%20Rev%202%20from%20DO C.pdf>

14. R.E. Einziger, H.C. Tsai, M. C. Billone, , B.A. Hamilton, Proc. of ICONE10, 10th Int. Conf. on Nucl. Eng., Arlington, VA, April 14-18, 2002.
15. Transactions, SMiRT 16 paper #1309, Washington DC, Aug. 2001.
16. *Thick silicon strip detector Compton imager*, E.A. Wulf, B.F. Philips, W.N. Johnson, J.D. Kurfess, E.I. Novikova, IEEE Trans. Nuc. Sci., **51**, pp.1997-2003, 2004.
17. *4 pi Compton imaging using a 3-D position-sensitive CdZnTe detector via weighted list-mode maximum likelihood.*, C.E. Lehner, Zhong He, Feng Zhang. IEEE Trans. Nuc. Sci., **51**, pp.1618-1624, 2004.
18. *Gamma-ray imaging with position-sensitive HPGe detectors*, K. Vetter, M. Burks, L Mihailescu, NIM A, **525**, pp.322-32, 2004.